

Delft University of Technology
Faculty of Applied Sciences
Faculty of Electrical Engineering, Mathematics and Computer Science
Department of Mathematical Physics

Exoplanet Cartography Using Light Curves With Multiple Reflection Models

by

Timo Gort
4804945

Supervisors:

Dr. P.M. Visser
Dr. A.J.L. Adam

Delft, July 22, 2022

Committee members:

Dr. A. Endo
Dr. K.P. Hart

BSc Thesis for Applied physics and
mathematics
TU Delft

Abstract

Context. In the near-future, exoplanets can be observed directly through telescopes. Although the resolution of the planet's image will only be one pixel at first, the intensity of this pixel will change over time because of the orbit around its host star and its diurnal rotation. This intensity as a function of time is called the light curve of an exoplanet. The changes in the light curve as a result of annual and diurnal rotation can in turn be used to obtain information about the surface of the planet, this is called spin-orbit tomography.

Aims. The aim of this study is to determine if an exoplanet's surface can be retrieved from its light curve for planet surfaces that can be described by Lambertian, Lommel-Seeliger or Fresnel reflection, or a combination of these. The variation in the light curve due to differences in the planet's surface will be used to find a map of its continents and oceans and to determine what surface types the planet is made of.

Methods. This thesis starts by composing a near-equal area segmentation of a sphere to maximize the retrieval of information per pixel of the exoplanet's surface. Additionally, a method for generating artificial planets is described, such that the following method can be tested on light curves, since the current telescopes are not powerful enough to measure an exoplanet's light curve. A linear transformation from the surface to the light curve is constructed to obtain the light curve from the surface. Consequently, this transformation is inverted in order to obtain information about the surface from the light curve. This method is applied to exoplanets with a stationary surface, i.e. no clouds or changing ice caps and is consistent of the following surfaces: water, vegetation, sand and snow, each described by a different reflection model. Lastly, surface retrieval is tested from a light curve with a realistic amount of photon shot noise ($\text{SNR} \approx 14$).

Results. The composed near-equal area segmentation of a sphere is the Voronoi diagram of the Fibonacci lattice. It is a very appropriate near-equal area segmentation, because the maximum difference in facet area is 12% for 1001 points. Furthermore, the retrieval of an exoplanet's surface from its reflected light curve is close to perfect for exoplanets that are described by a combination of the three reflection models if the light curve does not contain noise and there are a sufficient number of data points. If the light curve does contain shot noise, parts of the surface that are described by the Lommel-Seeliger law, are not retrieved correctly. However, the general shape of the surface that is described by Lambertian or Fresnel reflection is still retrieved correctly. If the surface can be described by one single reflection model, the planet's features are retrieved correctly from a light curve with shot noise regardless of the reflection model.

Conclusions. Spin-orbit tomography in the form of a linear transformation between the light curve and albedo map of an exoplanet is a very accurate method to retrieve the albedo map from a single observed pixel, even with a realistic amount of shot noise.

Contents

1. Introduction	1
2. Mapping of a sphere	3
2.1 Fibonacci lattice	3
2.2 Comparison between the Delaunay triangulation and Voronoi diagram of a Fibonacci lattice	6
2.3 Transforming a sphere into a 2-dimensional map	7
3. Generation of planetary maps with different types of surfaces	9
3.1 Albedo map generation	9
3.1.1 Generation of altitude map using tetrahedral subdivision	10
3.1.2 Creating an albedo map from an altitude map	11
4. Reflection of Light	14
4.1 Normalisation of the BRDF's	18
4.2 Fresnel reflection	19
4.3 Phase curves of a homogeneous exoplanet for different models	19
5. Light curve of an exoplanet	21
5.1 The coordinate system	21
5.2 Light curve of an exoplanet	21
5.3 The linear mapping for a combination of reflection models	25
5.4 Light curve with shot noise	26
6. Retrieval of the albedo map from an ideal signal	27
6.1 Inverting the transformation matrix	27
6.2 Albedo map retrieval for individual reflection models	27
6.3 Surface map retrieval using multiple reflection models	28
6.3.1 Retrieval with continuous albedo values	34
6.4 Surface map retrieval from signal with shot noise	37
6.4.1 Albedo retrieval for individual reflection models with shot noise . .	37
6.4.2 Retrieval of surface map from a signal with shot noise	39
7. Conclusion	43
References	45
A. Appendix	47
A.1 Normalisation of BRDF's	47
A.2 Link to GitHub repository	47

1. Introduction

There are many signs that extraterrestrial life has had many chances to develop and exist, but no signs of such life have been detected yet. This is the essence of the Fermi paradox: where are they?. It has nevertheless been shown that, statistically, most stars have planets orbiting them (Howard et al. (2010), Bryson et al. (2020)). In fact, Dressing and Charbonneau (2015) and Tuomi et al. (2014) have shown that a significant amount of M-dwarfs, stars with a maximum surface temperature of 3900 K and $0.6 M_{\odot}$, have planets inside their habitable zone. That is, within the zone where liquid water can be present given a sufficient atmospheric pressure.

Still, exoplanets are too small and too distant to be detected using direct imaging. Currently, their existence is inferred through transit observation (e.g. Borucki et al. (2011)), gravitational micro-lensing (e.g. Cassan et al. (2012)) or using the star's radial velocity (e.g. Mayor and Queloz (1995)). Issue is, these methods do not give any information about the properties of the planet's surface.

In the near-future though, exoplanets will be able to be detected by telescopes as one pixel. Nonetheless, besides the low resolution, there is another problem with the direct imaging of exoplanets. Compared to their sun, planets are extremely dim. When detecting Earth from interstellar space, the Sun is approximately 10 billion times brighter than Earth. A solution for this is coronagraphy, which essentially dims the perceived light of the star and in turn allows its planets to be visible. The first telescope that will do this in practice is the Nancy Grace Roman Space Telescope (Romero-Wolf et al. (2021)) due to launch in 2026.

Hence, assuming that we can observe exoplanets as one pixel, the only information that can be induced from it comes from the changing total amount of light reflected and scattered by the planet as it orbits its host star. This results in a change in brightness of the observed pixel, of which the brightness as a function of time is called the light curve. The light curve mainly changes because of two processes: the orbit around an exoplanet's star and changes in the illuminated surface as a result of the diurnal rotation of the planet. Fujii and Kawahara (2012) have shown that the derivation of a planet's albedo map from the light curve, called spin-orbit tomography, works on specific configurations of exoplanets. Furthering this method, Stuger (2021) has shown that the surface of a stationary (no clouds or changing icecaps) diffusely reflective exoplanet in a circular orbit can be mapped very accurately, even with a realistic amount of photon shot noise.

In this thesis we aim to advance this research by first composing a near equal-area mapping of a sphere in order to maximize the significance of every pixel of the retrieved albedo map. Subsequently, different types of light reflection are considered and applied to the method of planetary map retrieval from their light curve as described in Stuger (2021). These reflection types include diffuse reflection, which is characteristic of snow, Fresnel reflection, which is characteristic of water, and lastly reflection described by the Lommel-Seeliger law, which is characteristic of rocky surfaces like the moon. Lastly, the effect of shot noise on the retrieval of an exoplanet's map is investigated.

The thesis will start with composing a near-equal area segmentation of a sphere from the Fibonacci lattice in section 2. Next, the generation of artificial planetary maps with dif-

ferent surface types is described. Then, different models describing light reflection and their characteristics are described in section 4. Subsequently, the generation of the light curve of the artificially generated exoplanets is characterised as a linear transformation in section 5. The inversion of the linear transformation is explained and applied to the generated light curve for a noiseless signal in section 6. Lastly, the retrieval of the planetary map from a signal with shot noise is investigated.

2. Mapping of a sphere

In order to create a method that retrieves the surface map of an exoplanet, the curved surface of the planet will be approximated by many flat facets. This way, we can use a method that can easily perform calculations on each part of the planet. By definition, planets are close to spherical (see Hogan (2006)), so we aim to approximate a sphere by many flat facets.

Traditionally Earth's surface is divided using the longitude-latitude lattice. In this lattice, all points are separated by equal angles of longitude and latitude, see figure 1. A surface can be made by making each point correspond to a flat rectangle. As illustrated in the figure, the point distribution for this lattice is not homogeneous. The density of points is much higher at the poles than at the equator. The largest facet in this segmentation of a sphere is roughly 29 times larger than the smallest facet.

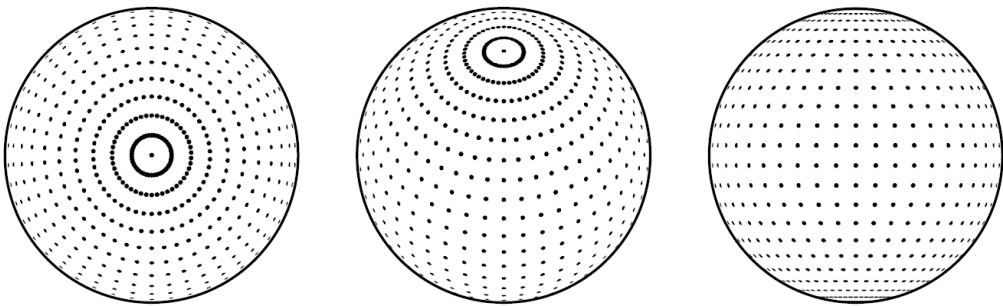


Figure 1: Mapping of points on a sphere using the longitude-latitude lattice for 1014 points. The left image is centered at the pole, the middle image is centered at latitude 45° and the right image is centered at the equator. (González (2009))

In this project, calculations will be done at each point, so it would be preferred to divide the surface into facets of equal area such that every part of the sphere is represented equally. Additionally, a lattice point should not be very stretched out, because then it will represent a part of the surface that is far away. If each facet is close to round, then each lattice point is a good representation for its facet.

Thus we need to divide the surface of a sphere into near-equal area facets that are close to circular. There is not one established way to do this, because a spherical surface can not be created using a finite number of flat discs. Because of this, a number of different methods have been contrived that try to approach these criteria. The method that will be used for this project is based on the Fibonacci lattice. This method is described in the following paragraph.

2.1. Fibonacci lattice

As the name implies, this lattice is based on the Fibonacci sequence. In this sequence, every element is the sum of the previous two, starting at 0 and 1 this sequence is: 0, 1, 1, 2, 3, 5, 8, 13, 21, The ratio between element n and element $n - 1$ approaches the golden ratio $\phi_g = \frac{1+\sqrt{5}}{2}$ as n approaches infinity.

Any odd number of points can be distributed near homogeneously over a sphere using the Fibonacci lattice such that one point is exactly on the equator (González (2009)). If

$2N + 1$ points are distributed, a point has longitude $\theta = 2\pi i \phi_g$ and colatitude $\phi = \arcsin(\frac{2i}{2N+1})$, for $i \in \{-N, -N+1, \dots, N-1, N\}$. Conceptually, every next point is lowered $\frac{2}{2N+1}$ in the vertical direction, resulting in a latitude decrease of $\arcsin(\frac{2}{2N+1})$, while the point is rotated around the vertical axis by an angle of $2\pi\phi_g$. The points are aligned in such a way that one point is exactly on the equator, resulting in no point occupying either pole. The final lattice is shown in figure 2.

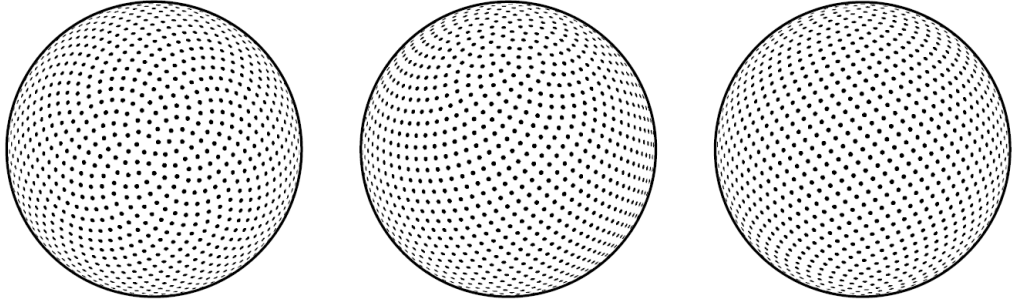


Figure 2: Mapping of points on a sphere corresponding to the Fibonacci lattice of 1001 points. The left image is centered at the north pole, the middle image is centered at latitude 45° and the right image is centered at the equator. The distribution looks very homogeneous, more so than the latitude-longitude lattice. (González (2009))

Constructing a segmentation of a sphere from these points is not as straight forward as for the latitude-longitude lattice. There are two main methods to do this, the Delaunay triangulation and the Voronoi diagram of the set of points.

In two dimensions, the Delaunay triangulation of a set of points \mathcal{P} is defined as a triangulation $DT(\mathcal{P})$ such that no point in \mathcal{P} is inside the circumcircle of any triangle in $DT(\mathcal{P})$ (Loera et al. (2010)). An example of the Delaunay triangulation of a set of points in two dimensions is shown in figure 3 by the solid lines. For a sphere, the Delaunay triangulation of points on its surface is equivalent to the convex hull of the set of points (Aurenhammer (1991)).

The Voronoi diagram is another way to divide a surface into facets on the basis of a set of points. The Voronoi diagram of a set of points, also called seeds, assigns a cell to each seed. For every location in a cell, the corresponding seed is the closest seed. The Voronoi diagram of a set of points in two dimensions is shown in figure 3 in dashed lines. The Delaunay triangulation of the Fibonacci lattice of 1001 points is shown in figure 4 and the Voronoi diagram of the Fibonacci lattice of 1001 points is shown in figure 5.

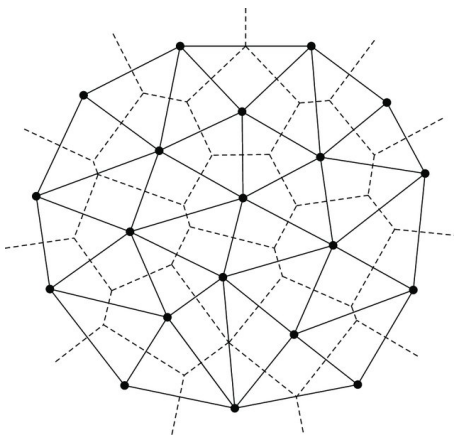


Figure 3: Delaunay triangulation (solid lines) and Voronoi diagram (dashed lines) for a set of points. Uwitonze et al. (2018)

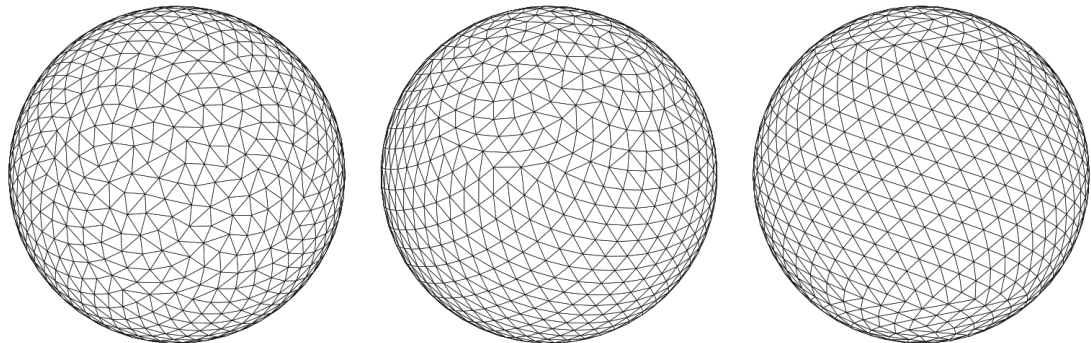


Figure 4: Delaunay triangulation and convex hull of the Fibonacci lattice for 1001 points, it consists of 1998 facets. The left image is centered at the north pole, the middle image is centered at latitude 45° and the right image is centered at the equator.

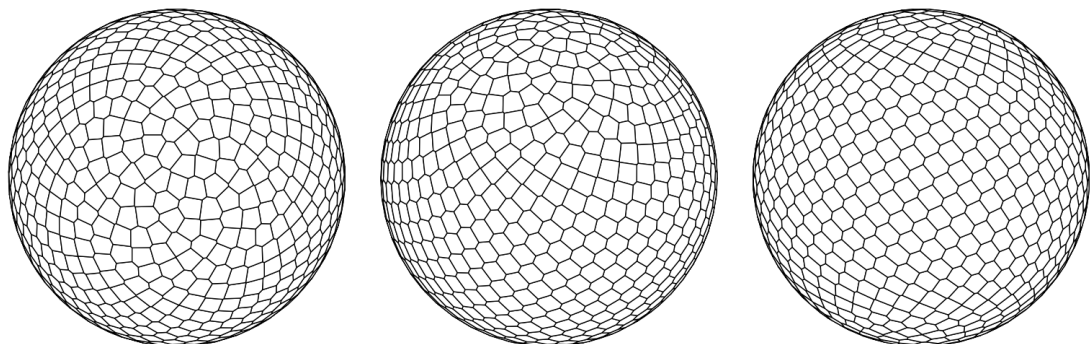


Figure 5: Voronoi diagram of the surface of the Fibonacci lattice for 1001 points. The left image is centered at the north pole, the middle image is centered at latitude 45° and the right image is centered at the equator.

2.2. Comparison between the Delaunay triangulation and Voronoi diagram of a Fibonacci lattice

A comparison between the two methods for creating a segmentation of a sphere from a Fibonacci lattice by assessing the previously discussed criteria; the facets should be near-equal area, and the facets should be close to circular. At first glance, the facets of the Voronoi diagram of the Fibonacci lattice look more circular than the Delaunay triangulation, suggesting that the Voronoi diagram would be a better method. To gain insight into the performance on near-equal area facets, the variation of the area of the facets is compared. For a Fibonacci lattice with 1001 points the Voronoi diagram consists of 1001 facets and the Delaunay triangulation consists of 1998 facets. A histogram of the area of each facet relative to the average area of the facets is given for both methods in figure 6. The horizontal axis shows that the Voronoi diagram has a much smaller deviation from the average than the Delaunay triangulation. To demonstrate this difference, the fraction between the maximal area of a facet A_{\max} and the minimal area of a facet A_{\min} can be used; $\frac{A_{\max}}{A_{\min}}$. This fraction is 1.58 and 1.12 for the Delaunay triangulation and Voronoi triangulation respectively.

Moreover, the standard deviation of the relative area for the Delaunay triangulation and the Voronoi diagram are $29 \cdot 10^{-3}$ and $6.9 \cdot 10^{-3}$ respectively. This makes sense, because every facet of the Voronoi diagram essentially is made out of parts of the triangles from the Delaunay triangulation. Thus the area of a facet of the Voronoi diagram is the average of the area of the corresponding triangles divided by three. Since the standard deviation of the Voronoi diagram is much smaller than the standard deviation of the Delaunay triangulation, it is better to use the Voronoi diagram of the Fibonacci lattice for our purpose.

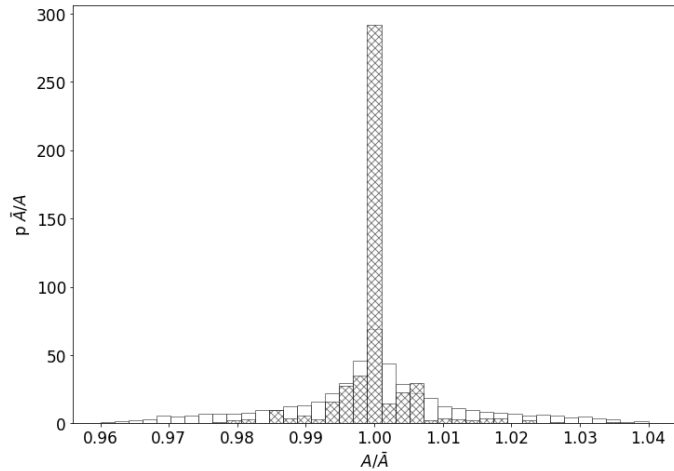


Figure 6: Histogram of the relative area of the facets for the Delaunay triangulation (blank) and the Voronoi diagram (crossed) of the Fibonacci lattice with 1001 points. The vertical axis represents the probability density function. Note that the bin at relative area 1 of the Delaunay triangulation is at around 70 of the vertical axis.

2.3. Transforming a sphere into a 2-dimensional map

For the purpose of showing maps of exoplanets in this report, it is more suitable to show a map in its entirety at once. This is also a dilemma, because a sphere can not be mapped onto a 2-dimensional surface without warping the surface. Just as for the problem of dividing a sphere into equal-area facets, multiple solutions have been devised for this problem.

An adequate solution is the Mollweide projection. However, this projection still has distortions compared to the sphere it corresponds to. To gain insight into this distortion, Tissot indicatrices can be used. These are ellipses that are shown over the projection that correspond to circles on the sphere. These indicatrices show compression or expansion in the longitude or latitude at the center of the circle. The Mollweide projection of the Earth is shown in figure 7 with the Tissot indicatrices.

Combining the Voronoi diagram of the Fibonacci lattice of 1001 points with the Mollweide projection and applying this to the Earth gives us the image shown in figure 8.

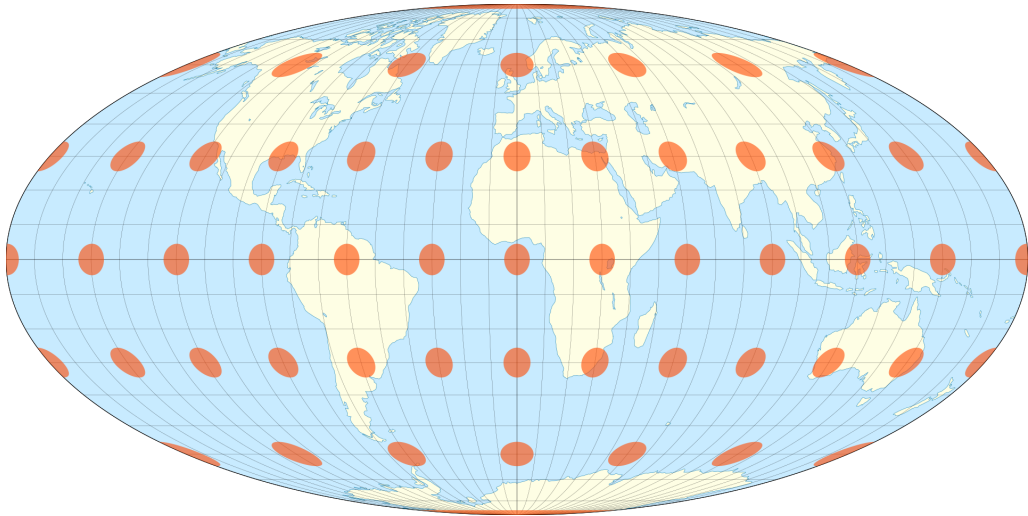


Figure 7: The Earth on a Mollweide projection with Tissot indicatrices overlaid. The Tissot indicatrices indicate how much the vertical and horizontal axis are warped in the middle of the point. Every ellipse corresponds to a circle with a diameter of 1000 km. (Kunimune (2018))

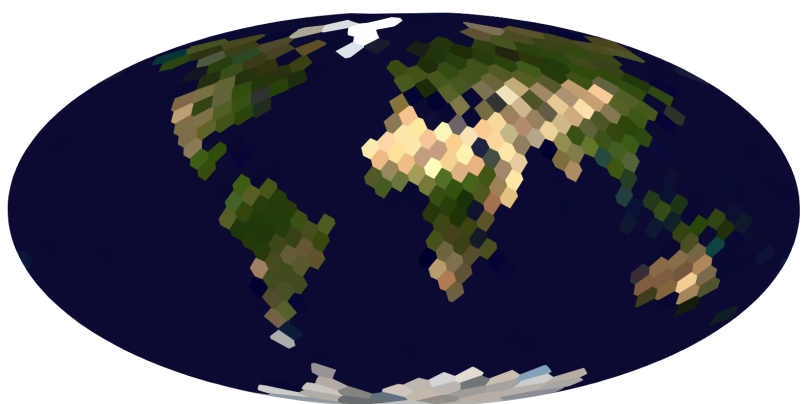


Figure 8: Mollweide projection of Earth based on the blue marble (Przyborski (2002)). The used facet area is the Voronoi diagram of the Fibonacci lattice with 1001 points.

3. Generation of planetary maps with different types of surfaces

Since the current telescopes are not powerful enough to observe exoplanets directly, there is no data yet from which we can retrieve the map of an exoplanet. Thus for this research, artificial planets will be created first. For that purpose, the concept of Bond albedo is introduced, hereafter the method for creating artificial planets is described.

The Bond albedo of a surface is the fraction of the total incident energy of electromagnetic radiation (light) that is scattered by the surface. Emitted radiation that is produced by the surface is not taken into account for the Bond albedo and the reflected radiation can not be negative, thus the Bond albedo is a value between 0 and 1. A ball of snow reflects a lot of light, so its Bond albedo is close to 1, while a black bowling ball that is not shiny absorbs most incident light, therefore its Bond albedo is close to 0.

From now on, Bond albedo will be referred to as albedo in this thesis. Albedo can also be defined for a specific light wavelength or range of light wavelengths. For example, a green leaf reflects more green light than red light, so its albedo is higher for green light than for red light. Telescopes measure light intensity for specific wavelengths, however in this thesis general albedo values are used to assess if the method works. When telescopes become powerful enough to observe exoplanets directly, the used albedo values for different surfaces can be modified to the wavelength or wavelengths of the telescope.

We need to know how much light reflects from each facet of the surface, we need to know three main properties of the surface facets: the area of each facet, the orientation, and the albedo. The area of the facets is calculated with the method described in section 2. For the orientation, we assume that the surface is approximately flat. This assumption is justified because the angle of the landscape in hilly areas is often small compared to the curvature of the planet, thus the amount of light reflected off a flat surface is approximately the same as the light reflected off the slightly inclined surface. Furthermore, this assumption also simplifies the model for the generation of the light curve of the planet significantly, because the inclination of the individual sub-surfaces does not have to be accounted for. Using this assumption on the orientation of each subsurface, the orientation is the plane perpendicular to the direction vector from the middle of the planet to the middle of the subsurface. Lastly we need to know the albedo of every subsurface. How this is done is described in the next subsection.

3.1. Albedo map generation

The albedo maps of fictional planets are made by first creating an altitude map by assigning an altitude to every facet of the surface. Altitude is correlated with surface type: if water oceans would be present, they would be at the lowest altitudes, snowy mountain peaks will in turn be at the highest altitudes. From these surface types, different albedo and reflection type can be inferred. The method for the retrieval of exoplanet's maps described in this thesis will be done on two types of albedo maps; discrete albedo maps and continuous albedo maps. For both maps the altitude map is first divided into different surface types. Then for the discrete albedo map, every facet that is of the same surface type is assigned the average albedo of the surface type. For the continuous albedo map, a range of albedo values is considered for every surface type and the assigned albedo value

of a facet is in this range and depends on its altitude.

3.1.1. Generation of altitude map using tetrahedral subdivision

The altitude maps are created using tetrahedral subdivision as described by Mogensen (2010) and Stuger (2021). This method is described in detail in algorithm 1. To determine the altitude of a point, the method starts by placing a tetrahedron around the entire Fibonacci lattice where every vertex has a corresponding altitude value. Then an iteration starts by adding a vertex in the middle of the longest edge with a new altitude value that is the average of the two neighboring vertices with a small added pseudo-random number. The tetrahedron containing the point is selected. If the longest edge of this tetrahedron is larger than resolution of the map, then the algorithm is repeated for this tetrahedron. If the longest edge of this tetrahedron is smaller than the resolution of the map, then the altitude of the point is the average of the altitudes of the final four vertices. Four height maps produced by this method are shown in figure 9.

An advantage of this method over other map generation methods is that this creates a spherical map without discontinuities. The main two reason are: the method is executed in three dimensions so there are no discontinuities because of a two dimensional map that is mapped onto a sphere; and secondly, the difference in altitude between two neighboring points scales with the distance between these points to the power $\frac{3}{2}$, since the sphere has radius 1, this distance is much smaller than 1 for most sphere mappings.

Algorithm 1 Tetrahedral subdivision

Input: a point p on the unit sphere for which to determine the altitude, an array v with the coordinates of the vertices of the starting tetrahedron that contains p , an array s with the seeds of every vertex from which to base the pseudo-random number on, and an array h of the altitudes of these vertices.

while $e_{max} < d_{min}$ **do**

1. Find the longest edge with length e_{max}
2. Rearrange the vertex array such that the edges of the longest edge are v_1 and v_2 .
3. Create new vertex v_{new} with

- $v_{new} = (v_1 + v_2)/2$
- $s_{new} = (s_1 + s_2)/2$
- $h_{new} = (h_1 + h_2)/2 + \text{random}(s_{new}) \cdot e_{max}^{\frac{3}{2}}/100$

Where $\text{random}(s_{new})$ creates a random number between -1 and 1 based on the seed s_{new}

4. If p is inside the convex hull of $\{v_{new}, v_2, v_3, v_4\}$, then set $v_1 = v_{new}$, $h_1 = h_{new}$ and $s_1 = s_{new}$. Otherwise set $v_2 = v_{new}$, $h_2 = h_{new}$ and $s_2 = s_{new}$.

end while

Output: $(h_1 + h_2 + h_3 + h_4)/4$, the altitude of p .

3.1.2. Creating an albedo map from an altitude map

Firstly, the altitude map is linearly scaled between 0 and 1. Subsequently, every facet is assigned a surface type depending on its height. The surface types that are considered in this thesis are water, vegetation, sand desert and snow. These surface types are chosen because of their prevalence on Earth and their indicative value of potential extraterrestrial life. It is assumed that the surface types are only correlated to altitude and not latitude, because they do not need to be perfectly realistic, we only need mock planets to test the method of spin-orbit tomography on. A facet with altitude h is water when $h \in [0, 0.5]$, it is vegetation if $h \in [0.5, 0.7]$, sand desert if $h \in [0.7, 0.9]$ and snow if $h \in [0.9, 1]$.

The surface types have a range of albedos, for example a rain forest has a lower albedo than a birch forest. This albedo range is applied to the continuous albedo map by scaling the albedo range linearly between the altitude values such that the lowest albedo value of the range a_{\min} is mapped to the lowest altitude of the surface type h_{\min} and the same for the maximum albedo and altitude. For every surface type, there is a most common albedo in its range on earth, which is used for the discrete albedo map. Water has a constant albedo of 0.06 NSIDC (2020), thus this value is used for both the continuous and the discrete albedo maps. The albedo values of the other surface types are summarised in table 1.

Table 1: Table containing the Albedo values of the used surface types. The albedo range is used for the continuous albedo maps and the discrete albedo is used for the discrete albedo maps. Kuusinen (2014), Tetzlaff (1983) and NSIDC (2020)

Surface type	Albedo range	Discrete albedo
Vegetation	[0.1,0.3]	0.15
Sand desert	[0.3,0.5]	0.4
Snow	[0.6,0.9]	0.8

The discrete and continuous albedo maps of the altitude maps in figure 9 are shown in figure 10 and 11 respectively.

Apart from the different albedo ranges of the different surface types, the way the surface scatters light can also differ. For example, a mirror reflects light differently than snow. How this works in detail, is described in section 4. This property can also be taken into account for the different surfaces, how this is done is described in section 5.

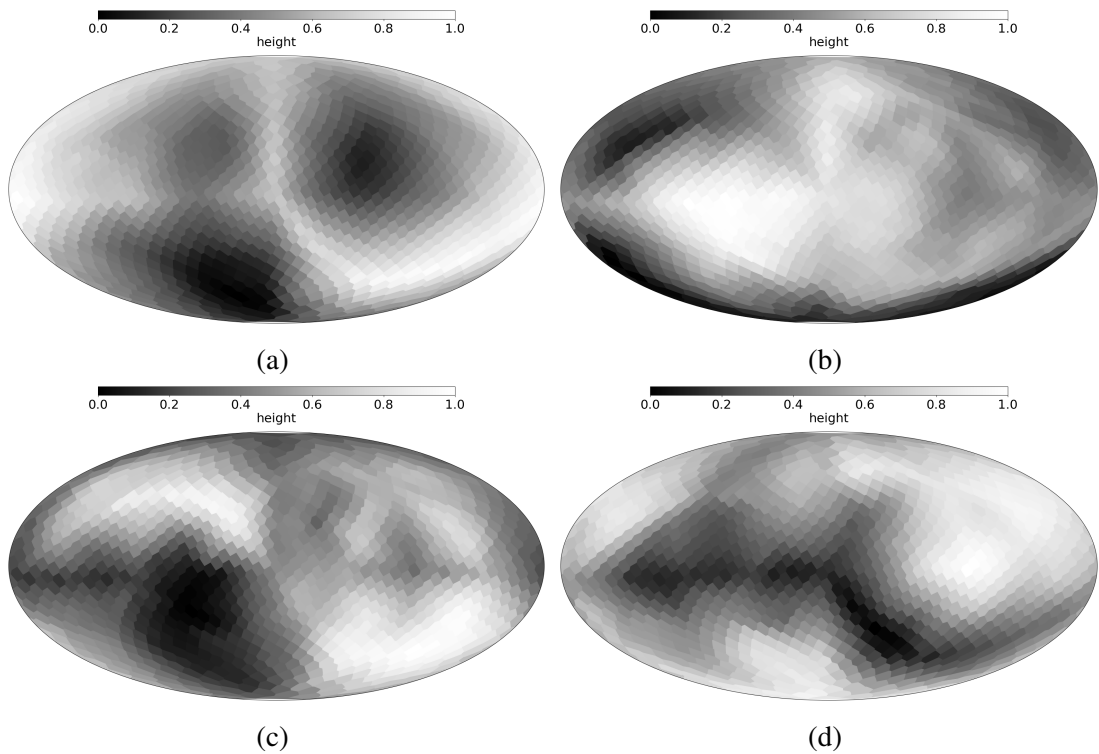


Figure 9: The height map of a fictional planet composed by the tetrahedral subdivision method.

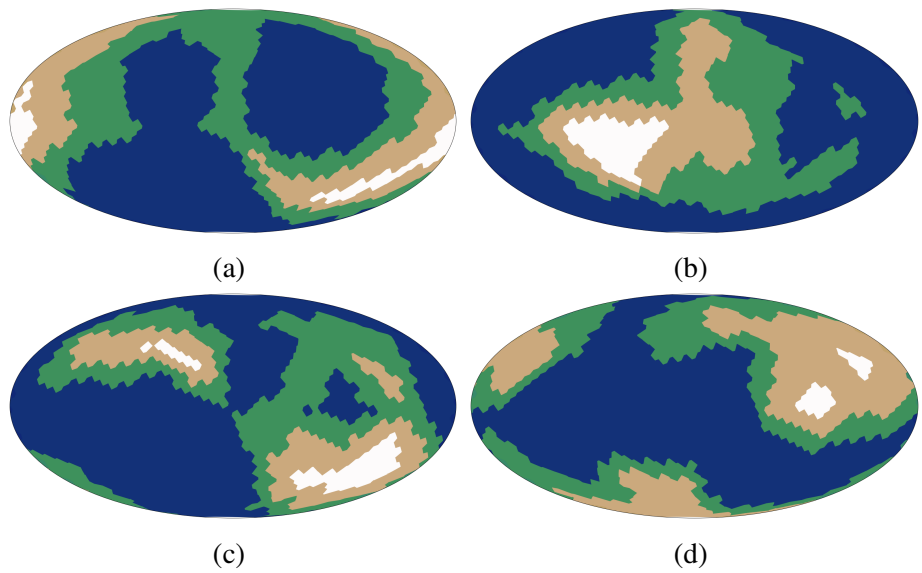


Figure 10: The discrete albedo maps of the artificial planets based on the height map of figure 9. The blue part represents water with an albedo of 0.06, green represents vegetation with an albedo of 0.15, light-brown represents sand desert with an albedo of 0.4 and white represents snow with an albedo of 0.8.

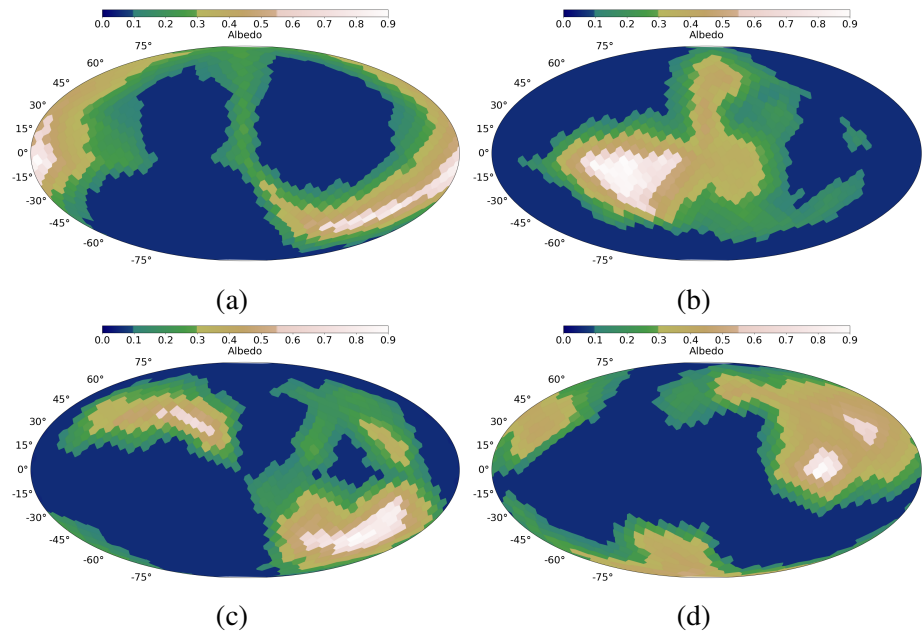


Figure 11: The continuous albedo maps of the artificial planets based on the height map of figure 9. The blue part represents water with an albedo of 0.06, green represents vegetation with an albedo ranging between 0.1 and 0.3, light-brown represents sand desert with an albedo between 0.3 and 0.5, and white represents snow with an albedo between 0.6 and 0.9.

4. Reflection of Light

In order to infer properties of a planet's surface from its light curve, it first has to be known how the surface reflects light. The analysis of this problem would be much easier if there is one formula that simulates the reflectance of all surfaces. However we can not use one formula for this, because different surface types reflect light differently. For example, the gas giant Jupiter reflects light differently than the moon as can be seen in figures 12 and 13. For the images at 0° phase angle, the edges of Jupiter appear darker than the middle, also called limb darkening. Phase angle is the angle between the direction of light from the host star to the exoplanet and the direction of light from the exoplanet to the observer. On the other hand, the full moon appears like a flat disk as seen figure 13. This demonstrates that a regolith body like the moon reflects light differently than a gassy body like Jupiter.

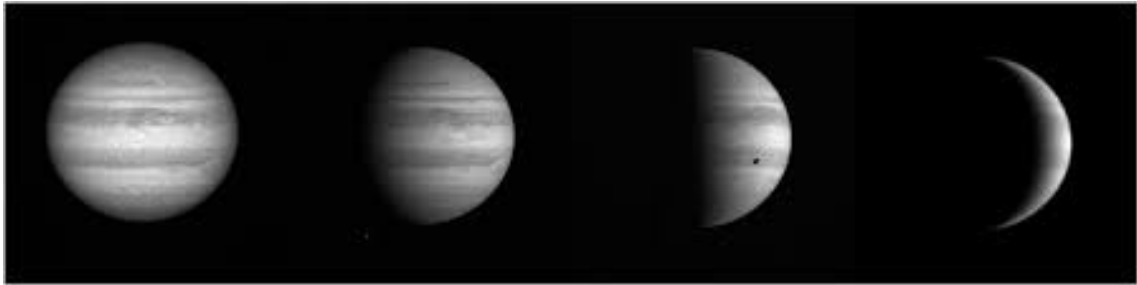


Figure 12: Jupiter at phase angles from left to right; 0° , 50° , 90° and 125° . In the image at 90° phase angle, the moon Io is in front of Jupiter. Note in the 0° phase angle image that limb darkening is apparent, this is characteristic of Lambertian reflection. (Mayorga et al. (2016))



Figure 13: The moon as seen from Earth at different phases. Note that the full moon appears like a flat disk, this indicates that the moon does not reflect light by Lambertian reflection. Wright et al. (2020)

Thus, before we can analyse the light curve of the planet, we need to know how light reflects from the planet's surface. For this purpose, we have considered multiple models that are characterised by f_{BRDF} known as the Bidirectional Reflectance distribution Function (BRDF). The BRDF gives the fraction between reflected radiance and incident irradiance dL_r/dE_i for a surface. Radiance $L \left[\frac{\text{W}}{\text{sr} \cdot \text{m}^2} \right]$ is the radiant flux per unit area per unit solid angle and irradiance $E \left[\frac{\text{W}}{\text{m}^2} \right]$ is the incident radiant flux per unit area. A schematic representation of what the BRDF describes is shown in figure 14.

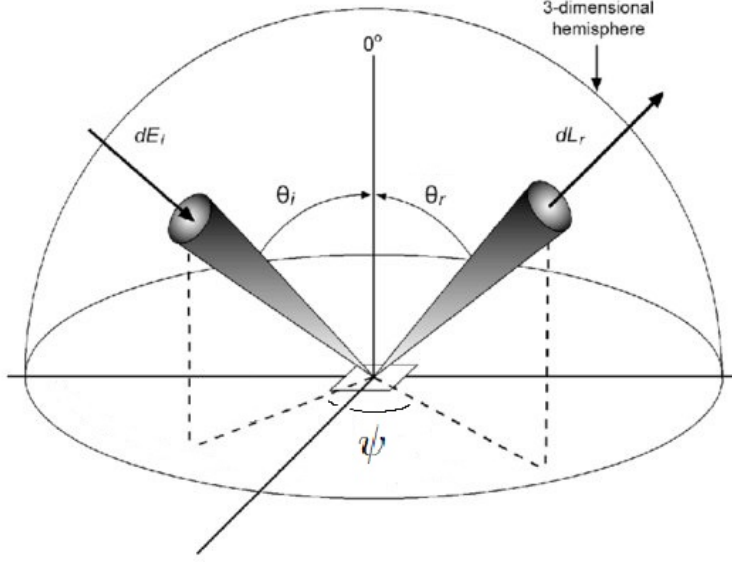


Figure 14: Parameters relevant to the BRDF; the fraction between the reflected radiance dL_r and incident irradiance dE_i for a surface. Here, θ_i , θ_r and ψ are the incident, emergent and azimuth angles respectively. (Schill et al. (2004))

The considered models are the Lambertian model, the Lommel-Seeliger model and the Fresnel reflection model. Fresnel reflection is specular reflection combined with the Fresnel coefficient, of which the details will be explained in more detail later. The BRDF's of the Lambertian, Lommel-Seeliger and specular models are shown in table 2. Here θ_i , θ_r and ψ are the incident, emergent and azimuth angles respectively, $\Delta\theta$ is the angle between the Fresnel reflection peak \vec{n}_r an the surface normal \vec{s} , lastly σ is the standard deviation of the Gaussian curve that is centered on the point where $\theta_i = \theta_r$. The angles are shown in figure 15. The Lommel-Seeliger model has been scaled such that a surface with albedo 1 exactly scatters all incident radiation energy on average for incident angles.

Table 2: Table with the bidirectional reflective distribution functions of the Lambertian, Lommel-Seeliger and specular reflection model.

Reflection model	$f_{\text{BRDF}}(\theta_i, \theta_r, \psi)$
Lambertian	π^{-1}
Lommel-Seeliger	$(4 \ln 2(\cos \theta_i + \cos \theta_r))^{-1}$
specular	$(4 \cos \theta_i \cos \theta_r \sqrt{2\pi} \sigma)^{-1} \exp \left\{ -\frac{1}{2} \left(\frac{\Delta\theta}{\sigma} \right)^2 \right\}$

The reflection of the Lambertian, Lommel-Seeliger and specular reflection model are shown in figure 16, 17 and 18 respectively for various phase angles α .

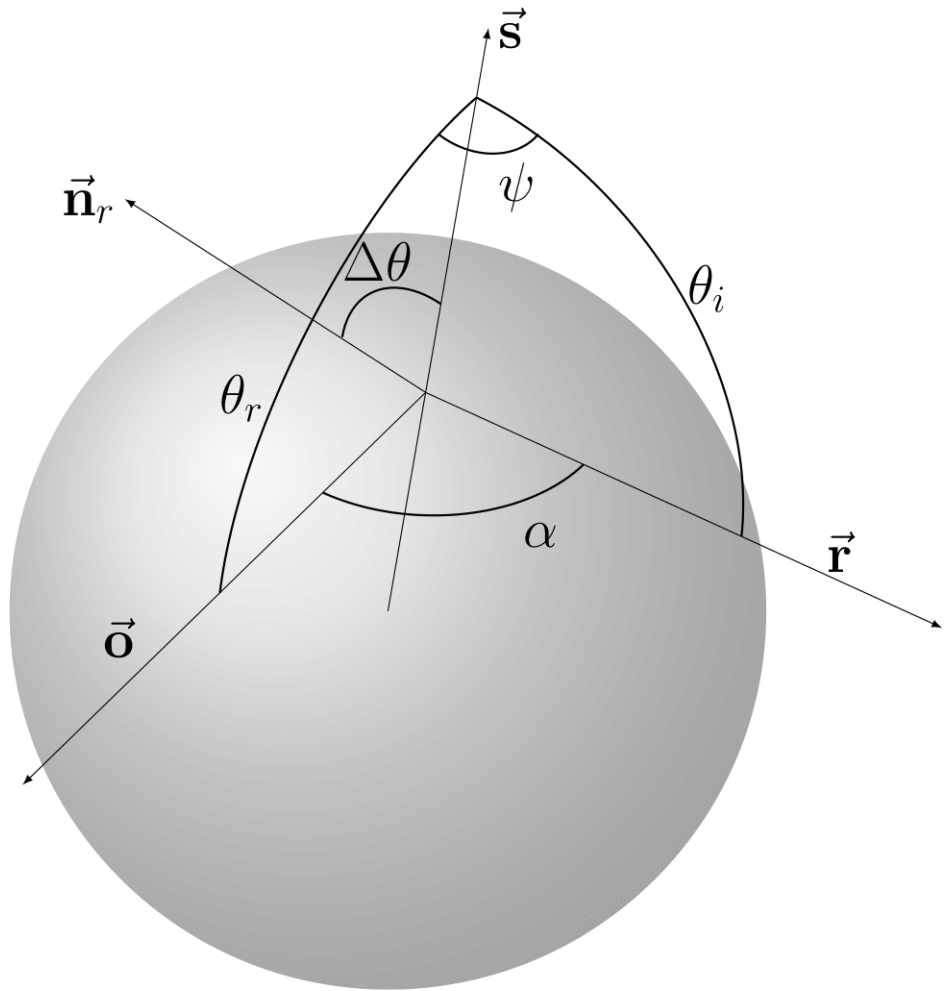


Figure 15: Schematic representation of the angles regarding given vectors from the planet to its host star \vec{r} , from the planet to the observer \vec{o} and surface normal \vec{s} . Here, \vec{n}_r is the direction vector of the reflection peak for Fresnel reflection. Here θ_i , θ_r and ψ are the incident, emergent and azimuth angles respectively, $\Delta\theta$ is the angle between the Fresnel reflection peak and the normal surface vector and α is the phase angle of the planet.

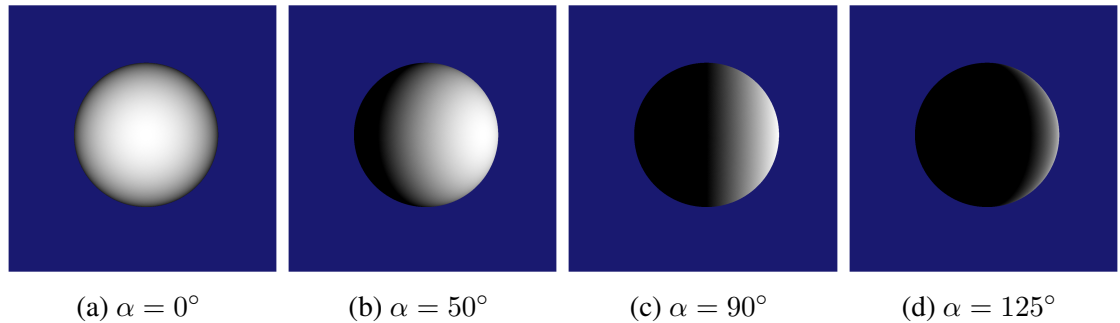


Figure 16: Light-intensity distribution on a homogeneous planet for Lambertian reflection for different phase angles α .

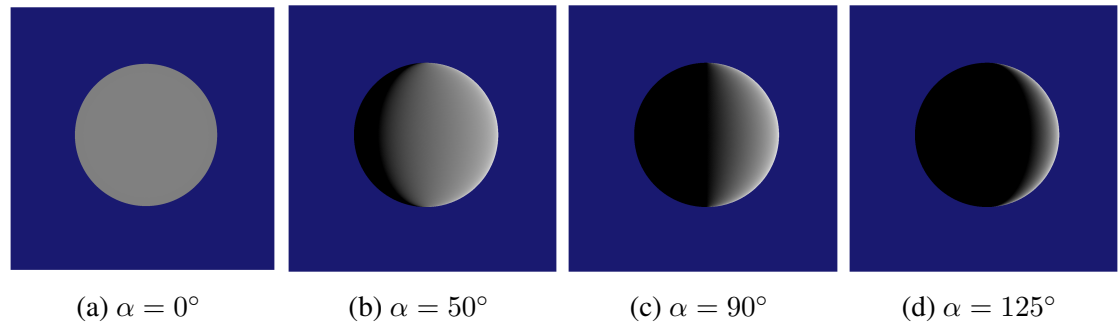


Figure 17: Light-intensity distribution on a homogeneous planet with the Lommel-Seeliger law for different phase angles α .

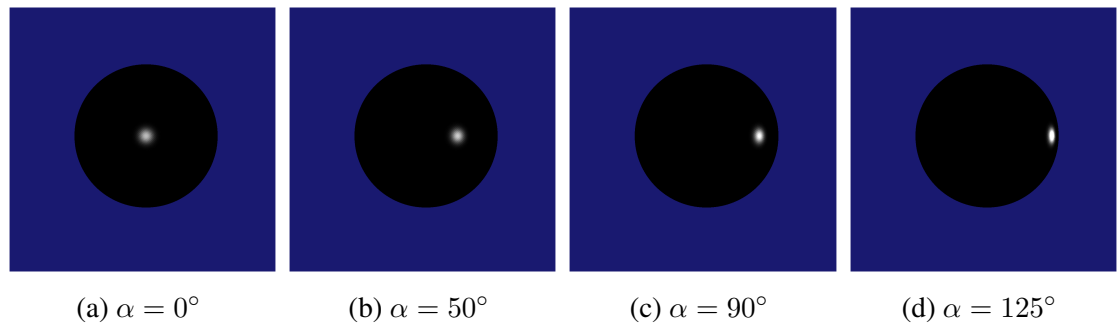


Figure 18: Light-intensity distribution on a homogeneous planet for Fresnel reflection for different phase angles α . Here, $\sigma = \frac{2\pi}{100}$ in the BRDF of Fresnel reflection shown in table 2.

4.1. Normalisation of the BRDF's

Before the BRDF's are used to create light curves, a normalisation step has to be in place. A BRDF is normalised when the total scattered light intensity from a point on the planet equal the incoming light intensity to this point. The fraction between the reflected light intensity and the incoming light intensity c_r is calculated with the following integral (Mungan (1998)):

$$c_r(\theta_i) = \int_0^{\frac{\pi}{2}} \int_0^{2\pi} f_{\text{BRDF}}(\theta_i, \theta_r, \psi) \sin \theta_r \cos \theta_r d\psi d\theta_r \quad (1)$$

If $c_r = 1$ then the model is normalised and is physically correct. On the other hand, if $c_r \neq 1$ then the model is not physically correct, because with an albedo of 1 then either not all incoming light is reflected or extra intensity is created. The normalisation is calculated for the Lambertian, Lommel-Seeliger in appendix A.1. The normalisation of the specular reflection BRDF is calculated numerically and can be found on the public GitHub repository¹. Of these models, only the Lambertian model is normalised for all incident angles. The value of c_r as a function of θ_i is shown in figure 19 for the Lommel-Seeliger and specular models.

Note that the Lommel-Seeliger law is scaled such that it is normalised on average for incident angle, and since the normalisation is not constant for all incident angles, the normalisation has parts above 1 and parts below. The specular reflection is normalised for angles smaller than 0.4π , this is as expected, because a spherical mirror reflects all light. The drop in reflected light at incident angles around $\frac{\pi}{2}$ is also sensible, because the Gaussian curve around \vec{n}_r is not fully visible as this point approaches the edge of the visible domain.

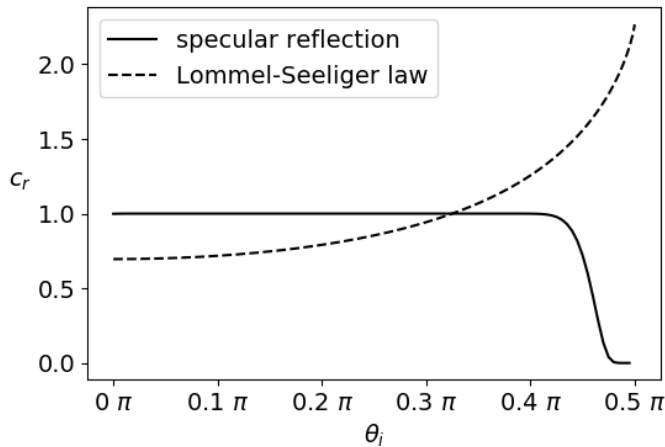


Figure 19: Fraction between total reflected light intensity and incident light intensity c_r as a function of the incident angle θ_i for the Lommel-Seeliger model in the dotted line and the specular model in the full line. The drop of the specular reflection near $\frac{\pi}{2}$ is caused by the fact that the visible circle drops behind the horizon for incident angles near $\frac{\pi}{2}$.

¹Link to GitHub repository: <https://github.com/SwederB/BEP-Exocartography>

4.2. Fresnel reflection

One surface type that will be used is water to model oceans on the surface of the planet. Water will be modeled by the specular model multiplied by the Fresnel coefficient R . The Fresnel coefficient depends on the polarisation of light and the refractive index of the first and second medium. In this case the Fresnel coefficient is used for light refraction from a vacuum to water at 25° C and unpolarised light. This Fresnel coefficient is the average of the Fresnel coefficient for s-polarised and p-polarised light, R_s and R_p respectively: $(R_s + R_p)/2$, of which the formulas are shown in equations 2 and 3 respectively. The average of these is plotted in figure 20 (Konijnenberg et al. (2021)). In practice, the variables needed to determine the Fresnel coefficient can be determined before the measurements of the light curve of the exoplanet. Thus, the assumed values do not impede the demonstration of application of this model when a planet has an ocean with different optical characteristics.

$$R_s(\theta_i) = \left| \frac{\cos(\theta_i) - 1.33\sqrt{1 - (\frac{1}{1.33}\sin(\theta_i))^2}}{\cos(\theta_i) + 1.33\sqrt{1 - (\frac{1}{1.33}\sin(\theta_i))^2}} \right|^2 \quad (2)$$

$$R_p(\theta_i) = \left| \frac{1.33\cos(\theta_i) - \sqrt{1 - (\frac{1}{1.33}\sin(\theta_i))^2}}{1.33\cos(\theta_i) + \sqrt{1 - (\frac{1}{1.33}\sin(\theta_i))^2}} \right|^2 \quad (3)$$

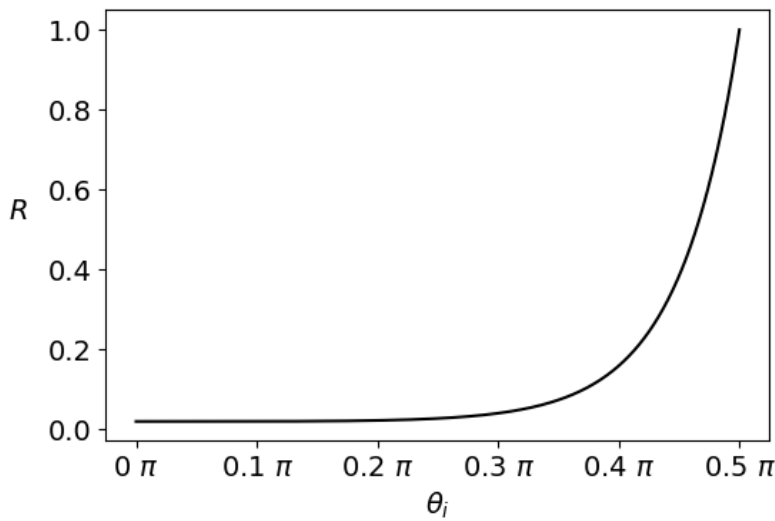


Figure 20: Plot of the Fresnel coefficient R to the angle of incidence θ_i for a refraction factor of $n = 1.33$ and neglected the effects of an atmosphere.

4.3. Phase curves of a homogeneous exoplanet for different models

The phase curve describes the perceived light of a body as a function of its phase angle. There are a lot of nearly homogeneous bodies in the solar system like the Moon, Jupiter and the Sun. Therefore, it is interesting to see what the phase curve of a homogeneous planet is for the different reflection models. This way, we can see what near-homogeneous

bodies in space are described by which model. The resulting phase curves are shown in figure 21.

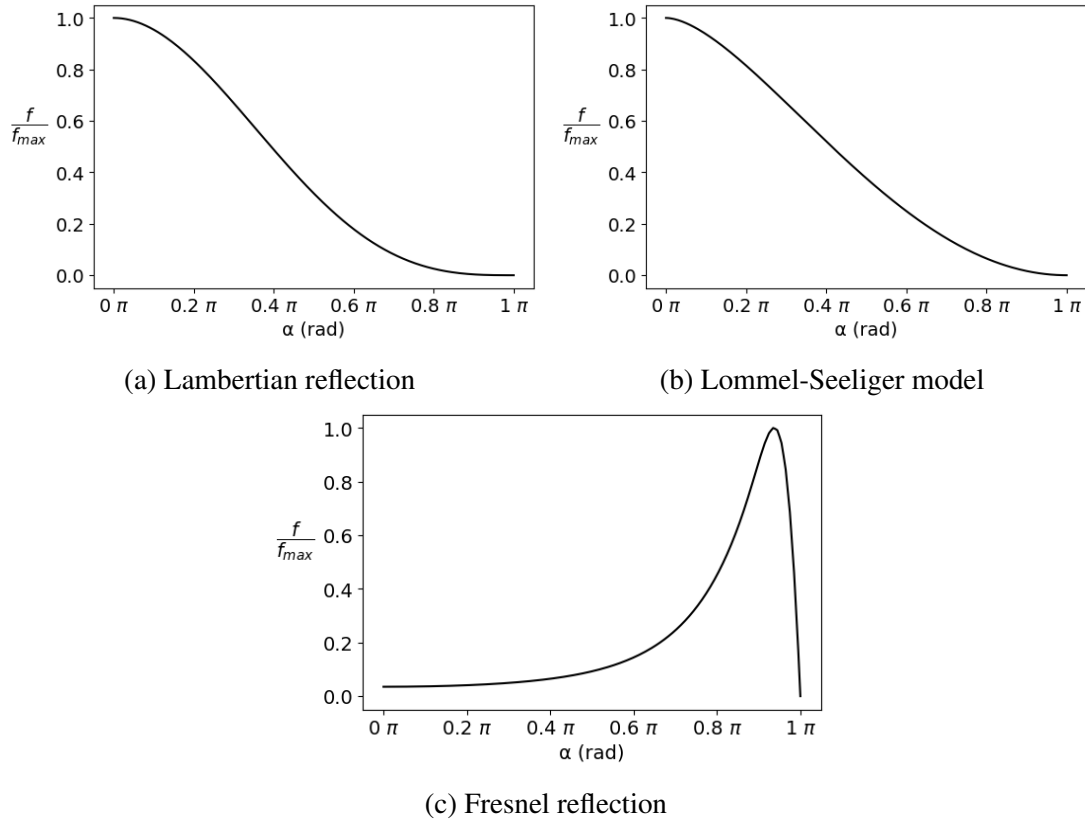


Figure 21: Phase curves of a homogeneous planet with albedo 1 for different reflection models. The vertical axis is scaled to the maximum value of the perceived light intensity and the horizontal displays the phase angle α . The Fresnel reflection is for light refraction from a vacuum to water at 25° C and unpolarised light with $\sigma = \frac{2\pi}{100}$ in the Fresnel BRDF (table 2).

5. Light curve of an exoplanet

In this section a coordinate system is defined such that the light curve of an arbitrary exoplanet can be analysed. Consequently, this light curve is composed numerically for the sphere mapping illustrated in section 2. In conclusion, the method for generating a light curve is applied to a fictional exoplanet constructed with the method illustrated in section 3.

5.1. The coordinate system

For the analysis of the reflection of light off the planet the coordinate system illustrated in figure 22 is used; the spherical planet with radius ρ orbits the star in the xy-plane in circular motion with angular velocity ω and radius R . The observer can be placed in the positive xz-plane, because there is symmetry with respect to this plane. This vector is time-invariant, so it does not need to have a y-component since the observed exoplanet is sufficiently far away. Furthermore, the planet rotates around its own axis $\hat{\mathbf{n}}$ with angular frequency Ω , $\hat{\mathbf{n}}$ is shown in equation 4. Here β_e is the equinox angle, which is the angle between the projection of $\hat{\mathbf{n}}$ onto the xy-plane and $\hat{\mathbf{x}}$. β_o is the obliquity of the planet, this is the angle between $\hat{\mathbf{n}}$ and $\hat{\mathbf{z}}$.

$$\hat{\mathbf{n}} = \begin{pmatrix} \cos \beta_e \sin \beta_o \\ \sin \beta_e \sin \beta_o \\ \cos \beta_o \end{pmatrix} \quad (4)$$

In addition, the vectors shown in equation 5 will be used to analyse the light curve of the planet. $\hat{\mathbf{o}}$ is the unit vector from the planet to the observer defined by γ the angle between the observer and $\hat{\mathbf{x}}$. $\hat{\mathbf{s}}$ the surface normal unit vector defined by spherical coordinates ϕ and θ . Lastly, $\hat{\mathbf{r}}$ is the unit vector from the planet to the star, where at time $t = 0$ the planet is on the positive x-axis.

$$\hat{\mathbf{o}} = \begin{pmatrix} \sin \gamma \\ 0 \\ \cos \gamma \end{pmatrix}, \quad \hat{\mathbf{s}} = \begin{pmatrix} \cos \phi \sin \theta \\ \sin \phi \sin \theta \\ \cos \theta \end{pmatrix}, \quad \hat{\mathbf{r}} = \begin{pmatrix} -\cos(\omega t) \\ -\sin(\omega t) \\ 0 \end{pmatrix} \quad (5)$$

5.2. Light curve of an exoplanet

In order to retrieve the surface of an exoplanet, we can not use direct imaging because the planet is only a pixel in our image. We only see the total light reflected at a given time. This signal is observed as the intensity of light, denoted by $f(t)$. The magnitude of this signal is the product of three terms; the light from the star that reaches the planet I_{in} , the fraction of light that is reflected by the surface in the direction of the observer, and the fraction of light from the planet that reaches the observer c_{obs} .

Let the star have total stellar power of I_0 and let the distance from the star to the planet be R , then the intensity of light that reaches an infinitesimal part of the planet's surface dA is $\frac{I_0}{4\pi R^2} \langle \hat{\mathbf{r}}, \hat{\mathbf{s}} \rangle d^2\Omega_s$, where $d^2\Omega_s$ is the solid angle of dA seen from the star. Thus the irradiance that reaches dA is $dE_i = \frac{I_0}{4\pi R^2} \langle \hat{\mathbf{r}}, \hat{\mathbf{s}} \rangle$. Furthermore, the radiance from dA is $dL_r = a_{dA} f_{BRDF} dE_i$ where a_{dA} is the bond albedo of dA and f_{BRDF} is the bidirectional

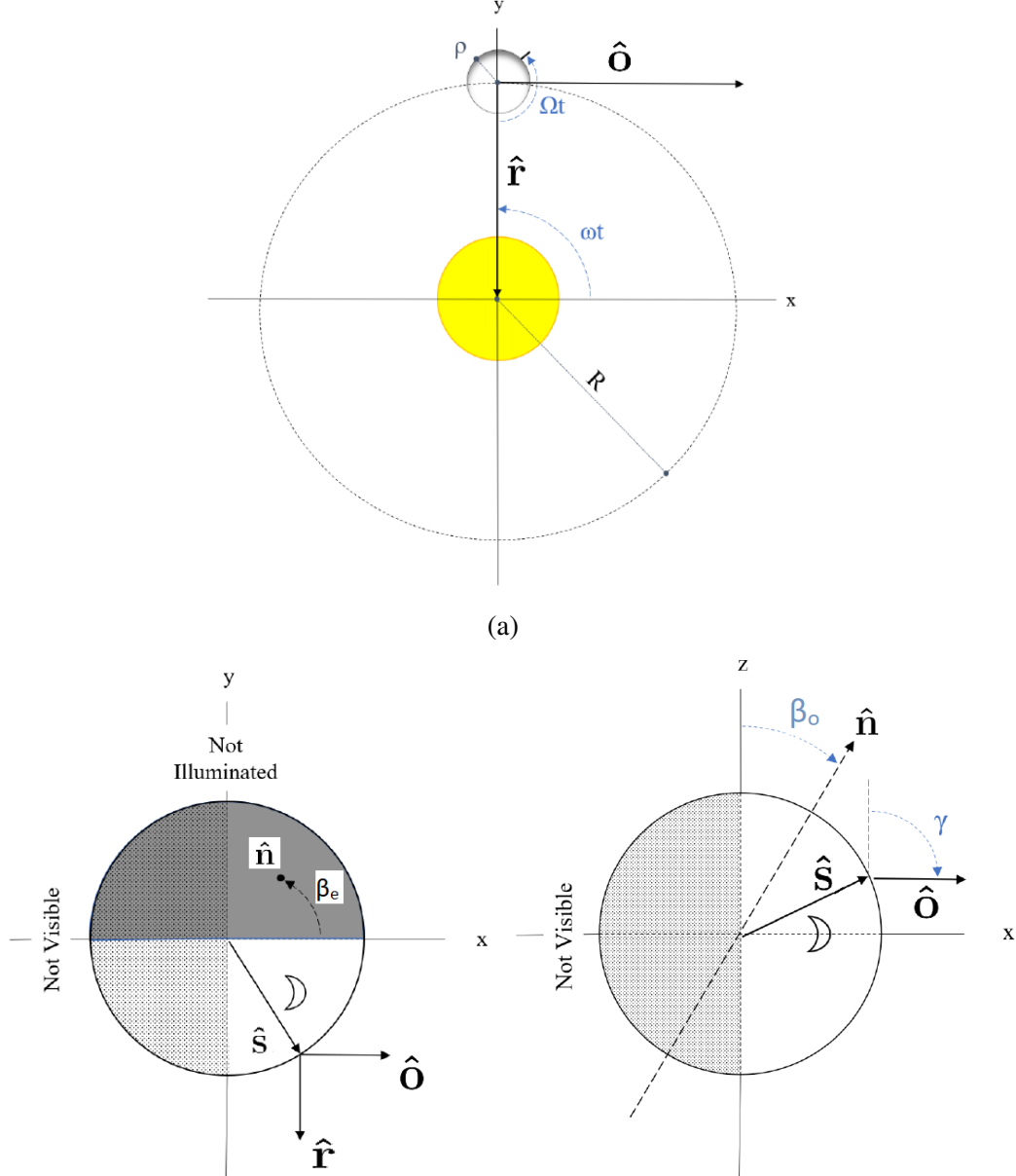


Figure 22: Schematic representation of the planetary system. The planet with radius ρ is in a circular orbit at a distance R around its host star with angular frequency ω . Furthermore, the planet rotates with angular frequency Ω about the axis $\hat{\mathbf{n}}$, defined by the obliquity β_o and equinox angle β_e . Moreover, at time t , the unit vectors from the planet to its host star and the observer are $\hat{\mathbf{r}}$ and $\hat{\mathbf{o}}$ respectively. $\hat{\mathbf{s}}$ is the unit vector perpendicular to the planet's surface. Lastly, \mathcal{D} is the observable domain that is both illuminated and visible by the observer. Images from Stuger (2021)

reflectance distribution function described in section 4. Lastly, the observed light intensity from dA is $I_{obs} = dL_r \langle \hat{\mathbf{s}}, \hat{\mathbf{o}} \rangle d^2\Omega_o dA$. Intensity of light is often measured relative to the star's measured intensity $I_0 d^2\Omega_o / 4\pi$ (Winn et al. (2008)), so the contribution of an infinitesimally small surface element dA of the planet to the light curve can be written as

$$f_{dA} = \frac{a_{dA} f_{\text{BRDF}}}{R^2} \langle \hat{\mathbf{r}}, \hat{\mathbf{s}} \rangle \langle \hat{\mathbf{s}}, \hat{\mathbf{o}} \rangle dA \quad (6)$$

Before we can construct the total light curve of the planet, we need to know what part of the surface contributes to the signal, since only a part of the planet's surface contributes to the signal at a time. Firstly, the observer can see the hemisphere that is facing their direction. From figure 22 it can be seen that for this hemisphere, the angle between $\hat{\mathbf{o}}$ and $\hat{\mathbf{r}}$ is between $-\frac{\pi}{2}$ and $\frac{\pi}{2}$, thus $\langle \hat{\mathbf{o}}, \hat{\mathbf{r}} \rangle \geq 0$. However, this hemisphere is not fully lit up by the star most of the time. Only the hemisphere that is lit up by the star can be seen, for this hemisphere the angle between $\hat{\mathbf{r}}$ and $\hat{\mathbf{s}}$ is between $-\frac{\pi}{2}$ and $\frac{\pi}{2}$, so $\langle \hat{\mathbf{r}}, \hat{\mathbf{o}} \rangle \geq 0$. Thus the part of the surface that contributes to the light curve, called the observable domain, is denoted by \mathcal{D} :

$$\mathcal{D} = \{ \langle \hat{\mathbf{r}}, \hat{\mathbf{o}} \rangle \geq 0 \wedge \langle \hat{\mathbf{s}}, \hat{\mathbf{r}} \rangle \geq 0 \}.$$

In order to obtain the total light curve at time t the integral of equation 6 is taken over the observable domain \mathcal{D} :

$$\begin{aligned} f(t) &= \frac{1}{R^2} \iint_{\mathcal{D}} a(\phi, \theta) \langle \hat{\mathbf{r}}, \hat{\mathbf{o}} \rangle \langle \hat{\mathbf{s}}, \hat{\mathbf{r}} \rangle f_{\text{BRDF}}(\hat{\mathbf{r}}, \hat{\mathbf{s}}, \hat{\mathbf{o}}) d^2\Omega_s \\ &= \frac{\rho^2}{R^2} \iint_{\mathcal{D}} a(\phi, \theta) \langle \hat{\mathbf{r}}, \hat{\mathbf{o}} \rangle \langle \hat{\mathbf{s}}, \hat{\mathbf{r}} \rangle f_{\text{BRDF}}(\hat{\mathbf{r}}, \hat{\mathbf{s}}, \hat{\mathbf{o}}) \sin(\theta) d\phi d\theta \end{aligned} \quad (7)$$

However, we have a finite resolution in our signal. If we also compute the planet's map with a resolution, the integral can be written as a matrix product:

$$\mathbf{f} = T\mathbf{a}. \quad (8)$$

Here $\mathbf{f} = [f(t_1), f(t_2), \dots, f(t_n)]$ is the signal where t_i is the time at measurement i , and $\mathbf{a} = [a_1, a_2, \dots, a_m]^T$ the Bond albedo at every pixel on the map, where the resolution of the signal and map is n and m respectively. T is the transformation matrix that maps the contribution of every surface part to every light measurement.

First, it has to be seen what the contribution of every surface part to every light measurement should be. For all time-steps, the coordinate (ϕ_j, θ_j) corresponding to vector $\hat{\mathbf{s}}_j$ corresponds to the same pixel in the coordinate system, so it does not point to the same surface element of the planet because $\hat{\mathbf{s}}_j$ does not rotate with the planet's rotation. To compensate for this, a number of rotations illustrated in figure 23 have to be performed. Firstly, for time step t_i the vector has to be rotated by Ωt_i radians around the z-axis for the planet's daily rotation, then it has to be rotated β_o and β_e radians around the y-axis and z-axis respectively to compensate for the planet's axial tilt. The vector that will always point to the same pixel on the planet's surface can be computed using the elementary rotation matrices:

$$\hat{\mathbf{s}}'_j = R_z(\beta_e) R_y(\beta_o) R_z(\Omega t_i) \hat{\mathbf{s}}_j \quad (9)$$

If $\hat{\mathbf{s}}'_j$ is not in the observable domain at time t_i , then either $\langle \hat{\mathbf{r}}_i, \hat{\mathbf{s}}'_j \rangle < 0$ or $\langle \hat{\mathbf{s}}'_j, \hat{\mathbf{o}} \rangle < 0$. In these cases we should have $T_{i,j} = 0$. To get an explicit expression of \mathcal{D} in T , we use the function $g^+ = \max\{0, g\} = \frac{1}{2}(g + |g|)$ on $\langle \hat{\mathbf{r}}_i, \hat{\mathbf{s}}'_j \rangle$ and $\langle \hat{\mathbf{s}}'_j, \hat{\mathbf{o}} \rangle$. Thus for time t_i and surface part $\hat{\mathbf{s}}_j$, the corresponding entry of T is;

$$T_{i,j} = \frac{\rho^2}{R^2} \langle \hat{\mathbf{r}}_i, \hat{\mathbf{s}}'_j \rangle^+ \langle \hat{\mathbf{s}}'_j, \hat{\mathbf{o}} \rangle^+ f_{\text{BRDF}}(\hat{\mathbf{r}}_i, \hat{\mathbf{s}}'_j, \hat{\mathbf{o}}) \sin(\theta_j) dA_j \quad (10)$$

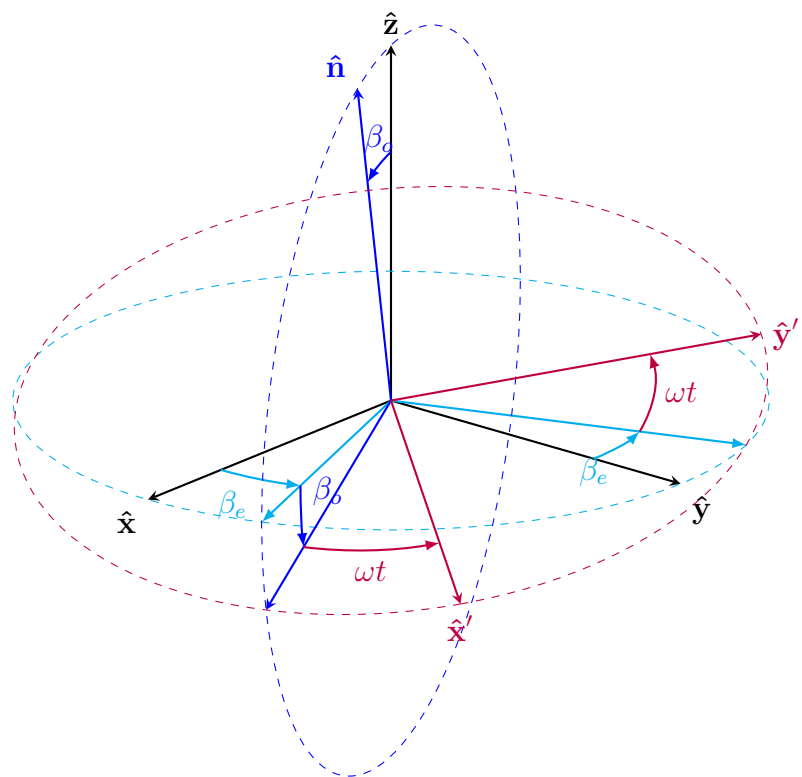


Figure 23: Figure based on Dorian (2017) illustrating how the planet is rotated according to its equinox angle β_e , obliquity β_o and diurnal rotation ωt .

The phase curves in figure 21 are constructed using a unity albedo vector, representing a homogeneous planet, indicating that the method returns logical light curves. To further illustrate this, consider the planet in figure 10(a). Using only Lambertian reflection, the light curve of this planet for three of its days around $\alpha = 0$ is shown in figure 24.

Even though the light reaching the planet is approximately constant, there are significant fluctuations in the light curve. This is exactly what is expected, because one side contains a lot of water with low albedo and the other side has a lot of high-albedo snow and sand. This argumentation can also be reversed. If this light curve is measured, we know that one hemisphere has a higher albedo than the other. Thus it is possible to infer properties of the planet's surface by only observing the light-curve.

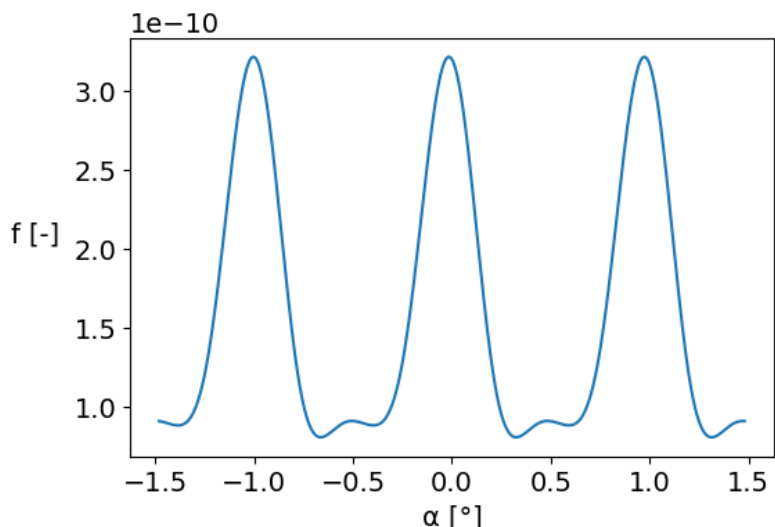


Figure 24: Light curve of the exoplanet shown in figure 10(a) for three days using only Lambertian reflection. The fraction between the intensity of the star and the intensity of the exoplanet is shown on the vertical axis, the phase angle α in degrees of the planet is shown on the horizontal axis. This planet's orbital period equals 365 diurnal periods.

5.3. The linear mapping for a combination of reflection models

The methods described previously only works for one reflection model at one time. In practice, the planets that are in our interest have different surface types with different reflective properties. This is solved by assigning multiple albedo values for a facet, one for every reflection model. For instance, if a surface is Lambertian and has 1 albedo, then the Lambertian albedo is 1 and the Fresnel and Lommel-Seeliger albedos are 0. Furthermore, if a surface is partly diffuse and partly specular, this property can be easily be accounted for using this method.

As a consequence, the albedo vector \mathbf{a} in equation (8) has an increased size. To keep the mapping from the albedo to the light curve a linear transformation, the albedo vector has to remain as a vector. It will now be

$$\mathbf{a} = \begin{bmatrix} \mathbf{a}_{La} \\ \mathbf{a}_{LS} \\ \mathbf{a}_w \end{bmatrix},$$

where \mathbf{a}_{La} , \mathbf{a}_{LS} and \mathbf{a}_w are the respective albedo vectors for Lambertian reflection, the Lommel-Seeliger model and Fresnel reflection. The corresponding change in the transformation matrix T is $T = [T_{La} \ T_{LS} \ T_w]$, where again T_{La} , T_{LS} and T_w are the transformation matrix corresponding to Lambertian reflection, the Lommel-Seeliger model and Fresnel reflection respectively. Thus, the mapping from the albedo vector to the light curve for the three discussed reflection models is:

$$\mathbf{f} = [T_{La} \ T_{LS} \ T_w] \begin{bmatrix} \mathbf{a}_{La} \\ \mathbf{a}_{LS} \\ \mathbf{a}_w \end{bmatrix} \quad (11)$$

5.4. Light curve with shot noise

Exoplanets are very far away, the closest star being at 4.2 light-years from the solar system. Since exoplanets are also very dim, the light intensity observed is very low. Because of this, the observed light will be subject to shot noise. Shot noise is caused by the discrete nature of light, the photons that make up a signal are not emitted at a constant rate. The number of photons emitted in a given time interval t_{int} is described by the Poisson distribution. Thus the probability that k photons are emitted is;

$$\mathcal{P}(k) = \frac{\bar{N}^k e^{-\bar{N}}}{k!} \quad (12)$$

where \bar{N} is the expected number of emitted photons.

The expected number of emitted photons in time interval t_n by an exoplanet is given by the following formula;

$$\bar{N} = \frac{8}{3} \dot{N}_{star} t_{int} \left(\frac{d}{4d_0} \right)^2 \left(\frac{\rho}{2R} \right)^2 \quad (13)$$

where \dot{N}_{star} is the total photon emission rate of the host star, d_0 is the distance from the planetary system to the observer, d is the diameter of the observing telescope and ρ and R are the radius of the exoplanet and its exoplanet around the host star respectively.

For an earth-twin in a twin solar system ($\rho = 6.4 \cdot 10^6$ m, $R = 1.5 \cdot 10^{11}$ m and power of the star $P_{star} = 3.8 \cdot 10^{26}$ W) with an observation time of 1 hour by the James-Webb telescope ($d_0 = 6.5$ m) at wavelength $0.4 \mu\text{m}$ at a distance of 5 light-years gives an expected number of photons $\bar{N} \approx 187$. This corresponds to a signal to noise ratio $\text{SNR}_{\max} = \sqrt{\bar{N}} \approx 14$. This is an upper bound of the signal to noise ratio for such a planet, because other sources of noise are also present, such as Gaussian noise caused by the measuring instrument, and background starlight that pollutes the signal. Furthermore, this expected number of photons is for an albedo 1 Lambertian planet that is observed with phase angle 0. To compensate for this, the expected number of photons is scaled linearly to the signal without noise.

6. Retrieval of the albedo map from an ideal signal

From the light curve of an exoplanet, its map can be retrieved. To achieve this, the transformation matrix, introduced in section 5, will be inverted to give a map from the light curve to the albedo vector. Consequently, the retrieval of planets that can be fully described by one reflection type, Lambertian, Lommel-Seeliger or Fresnel is tested. Thereafter, the reflection models are combined for a planet that consists of different surfaces that are each described by one of these reflection models.

The retrieval method is only done for edge-on observation of the planetary system in this thesis, however note that the angle of inclination γ can be set to fit any specific planetary system in the method.

6.1. Inverting the transformation matrix

Inverting matrix T is not trivial, because it is not necessarily square and if it is, its determinant can be zero so that T has no inverse. The dimensions of T are $(n_t, m \times n_s)$ where n_t is the number of measurements, m is the number of reflection models used and n_s is the number of pixels used for the mapping. Nevertheless, we can use the Moore-Penrose inverse, or pseudo inverse, that always exists.

The pseudo inverse of T can be computed by finding the singular value decomposition $T = U\Sigma V^T$ where U and V are orthogonal matrices and Σ is a rectangular diagonal matrix containing the positive non-zero singular values of T . The number of non-zero entries of Σ is equal to the rank of T . Consequently, the pseudo inverse of T is $T^+ = V\Sigma^+U^T$, where Σ^+ is the pseudo inverse of Σ , which is computed by taking the reciprocal of each singular value and transposing the matrix. However, some singular values could be very small but non-zero, because of noise or numerical errors, causing their reciprocal to be very large. A solution for this is to introduce a singular value cutoff (SVC) such that singular values smaller than the SVC are set to zero.

Using this pseudo inverse, the albedo map that is retrieved from the signal f is

$$\mathbf{a} = T^+f.$$

However, to compute T in the first place, the axial tilt of the planet has to be known and this can not be directly observed from its orbit. Among others, Stuger (2021) has shown that the axial tilt can be accurately determined for discrete albedo maps of Lambertian planets by minimizing the following distance: $\|f - T(\beta_e, \beta_o)T^+(\beta_e, \beta_o)f\|$. In order to focus on the map retrieval from a signal with shot noise, the axial tilt is assumed to be known from this method.

6.2. Albedo map retrieval for individual reflection models

The method described in the previous section is applied to three versions of the planet shown in figure 25(a). Every version of the planet reflects light by one of the three reflection models presented in section 4, then the albedo map is retrieved with the knowledge that the planet reflects light by the corresponding model.

The maps for the Lambertian and Lommel-Seeliger reflection are exactly as shown in figure 25(a); the surface is divided into four surface types with a corresponding albedo.

For the Fresnel reflection, the albedo vector \mathbf{a} does not represent albedo, it rather consists of binary values (0 or 1) indicating if there is water (1) at the corresponding facets or not (0). The resulting map is shown in figure 25(b), where white represents water and black represents land.

Using the transformation $\mathbf{f} = T\mathbf{a}$, the computed light curves of each version of the exoplanet without noise are shown in figure 26 with equinox $\beta_e = \frac{\pi}{2}$ and obliquity $\beta_o = \frac{\pi}{6}$. Notice that the maximal amplitude of a Lambertian planet is much higher than the other reflection types. So, if a planet has Lambertian, rocky and water parts, then at the right angles the Lambertian surface will be brighter in comparison.

Using the Moore-Penrose pseudo inverse of T with the light curves, the planet maps shown in figure 27 are retrieved.

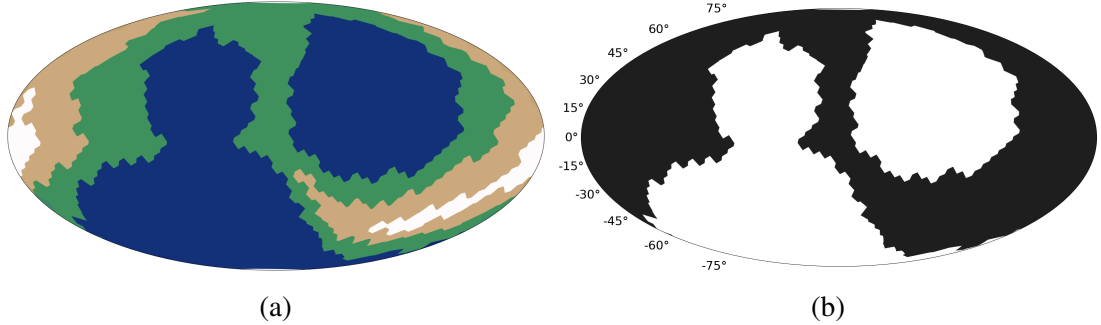


Figure 25: The discrete albedo map of the fictional planet (left) generated by tetrahedral subdivision described in section 3 and its water map (right). In the water map, black is land and white is water.

It is seen that the retrieval quality is close to perfect for the Lambertian and Lommel-Seeliger reflections. For Fresnel reflection, the water map is retrieved perfectly up to $\frac{\pi}{6}$ radians from the equator. However, the facets farther away are not retrieved correctly. But, because of the axial tilt of the planet, the facets that are more than $\frac{\pi}{6}$ radians from the equator never reflect light from the sun. As a result, the retrieved albedo of these facets is zero.

6.3. Surface map retrieval using multiple reflection models

In the previous paragraph it is shown that the retrieval of an exoplanet's albedo map can be done very accurately for individual light reflections. In this paragraph, a more realistic planet will be considered that consists of surfaces that are described by different light reflections.

The considered surface types are assigned the following albedo values for every model. Water has an albedo factor of 1 for Fresnel reflection, sand is 0.4 albedo for the Lommel-Seeliger model and finally snow has 0.8 albedo for the Lambertian model. Furthermore, leaves are neither fully diffuse nor fully specular, but a combination of the two (Grant (1987)). However, since most areas of vegetation consist of many leaves from plants and trees in different orientations, the Lambertian model is assumed to be a good approximation of the light reflection of vegetation and the albedo is 0.15. Using these values for the planet shown in figure 25(a), the light curve for edge-on observation is plotted in figure 28.

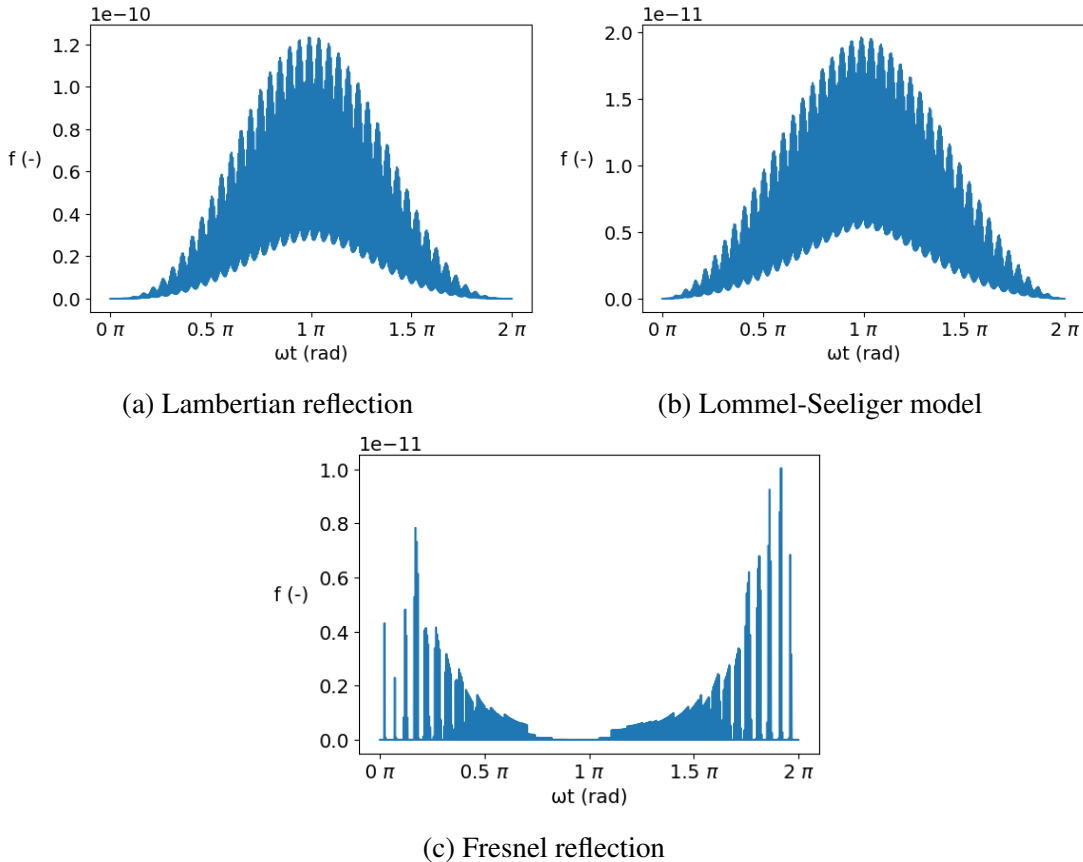


Figure 26: Light curves for edge-on observation of the fictional exoplanet shown in figure 25. The vertical axis shows the light-intensity relative to the planet’s host star and the horizontal axis shows the product of time t and the angular frequency of the planet’s orbit. Figure (a) shows the light curve when the planet reflects light diffusely, figure (b) shows the light curve when the Lommel-Seeliger law describes the planet’s reflection, and figure (c) shows the light curve when the water reflects light by Fresnel reflection and the land does not reflect light. For this planet’s orbit a day is 24 hours and there are 365 of these days in its year. The planet has an equinox angle $\beta_e = \frac{\pi}{2}$ and obliquity $\beta_o = \frac{\pi}{6}$. There are 1500 time measurements spread out evenly over the year.

Using the Moore-Penrose pseudo inverse of T on the light curve returns three albedo maps, one for every reflection type. These maps are shown in figure 6 with the map of the mean squared error (MSE) between the original and retrieved map for the corresponding reflection type.

Similar as for the albedo retrieval for individual reflection types, the Lambertian and Lommel-Seeliger maps are retrieved perfectly and the water map is only retrieved correctly up to 30° from the equator. This indicates that, with enough measurements, the different reflections can be distinguished from one light curve. With this information, the surface types can also be retrieved.

In our method, the retrieved surface type for a given facet is taken to be the one for which the distance between the retrieved albedo vector of the facet $\mathbf{a}_f = (a_{f,La}, a_{f,LS}, a_{f,w})$ and the albedo vector of the surface type $\mathbf{a}_s = (a_{s,La}, a_{s,LS}, a_{s,w})$ is minimal. Additionally, in ideal conditions water facets that never reflect a significant amount of light, return a zero albedo vector. Since no other considered surface type has a zero albedo vector, the

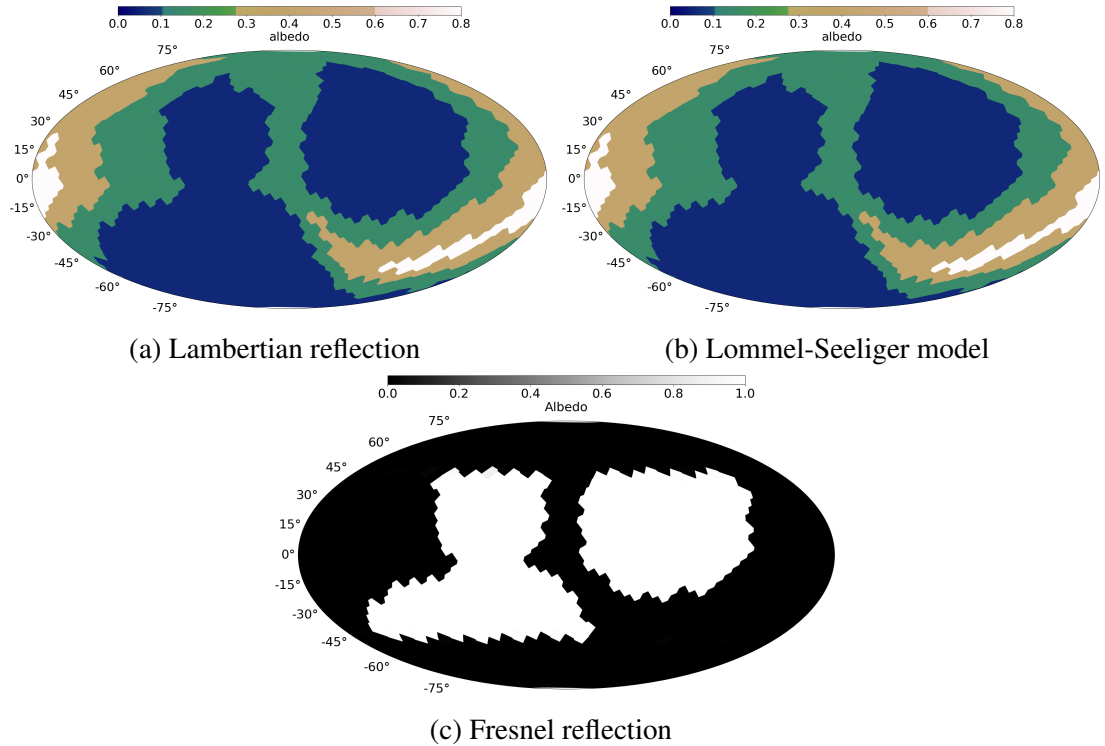


Figure 27: Retrieved albedo maps from the light curves shown in figure 26 with the knowledge of the reflection type of the planet. For Lambertian reflection and Lommel-Seeliger, the retrieved maps are identical to true map. For Fresnel reflection, the facets up to roughly $\frac{\pi}{6}$ radians from the equator are retrieved perfectly, but the other facets all have zero albedo. This is because the glint from the star does not reach these regions.

distance between the retrieved albedo vector and the zero vector is also considered for the determination of a water facet. So consider the retrieved albedo of $\mathbf{a}_f = (0.2, 0.4, 0.05)$, then the norm for water, vegetation, sand and snow is respectively 1.05 or 0.45, 0.41, 0.21 and 0.72, so the retrieved surface type is taken to be sand as the norm of the difference is the smallest. Using this method, the planet map that is retrieved is shown in figure 30.

From all facets, only one out of the 1001 has been assigned the wrong surface type when the signal is ideal; a water facet is retrieved as vegetation. This shows that the method also works very well for a more realistic planet with a small number of different surface types.

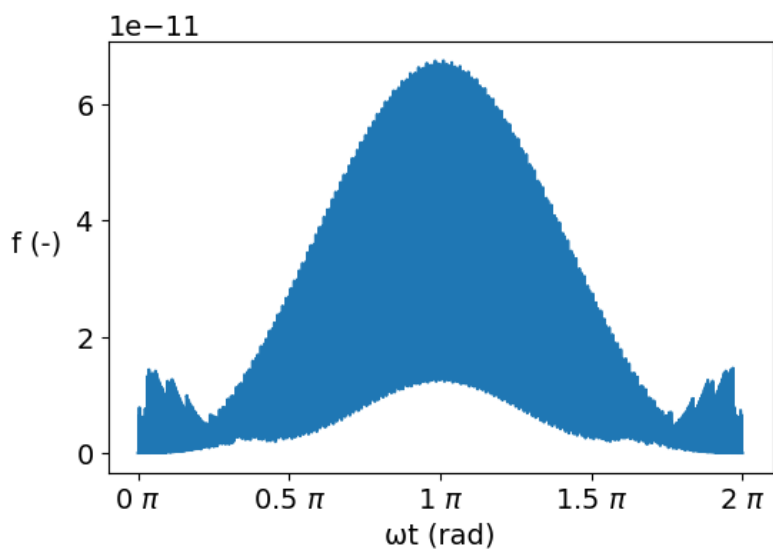


Figure 28: Light curve for noiseless edge-on observation of the planet shown in figure 10(a) using Lambertian reflection for the vegetation and snow, the Lommel-Seeliger for sand, and Fresnel reflection for water. For this planet's orbit a day is 24 hours and there are 365 of these days in its year. The planet has an equinox angle $\beta_e = \frac{\pi}{2}$ and obliquity $\beta_o = \frac{\pi}{6}$. There are 3500 time measurements spread out evenly over the year.

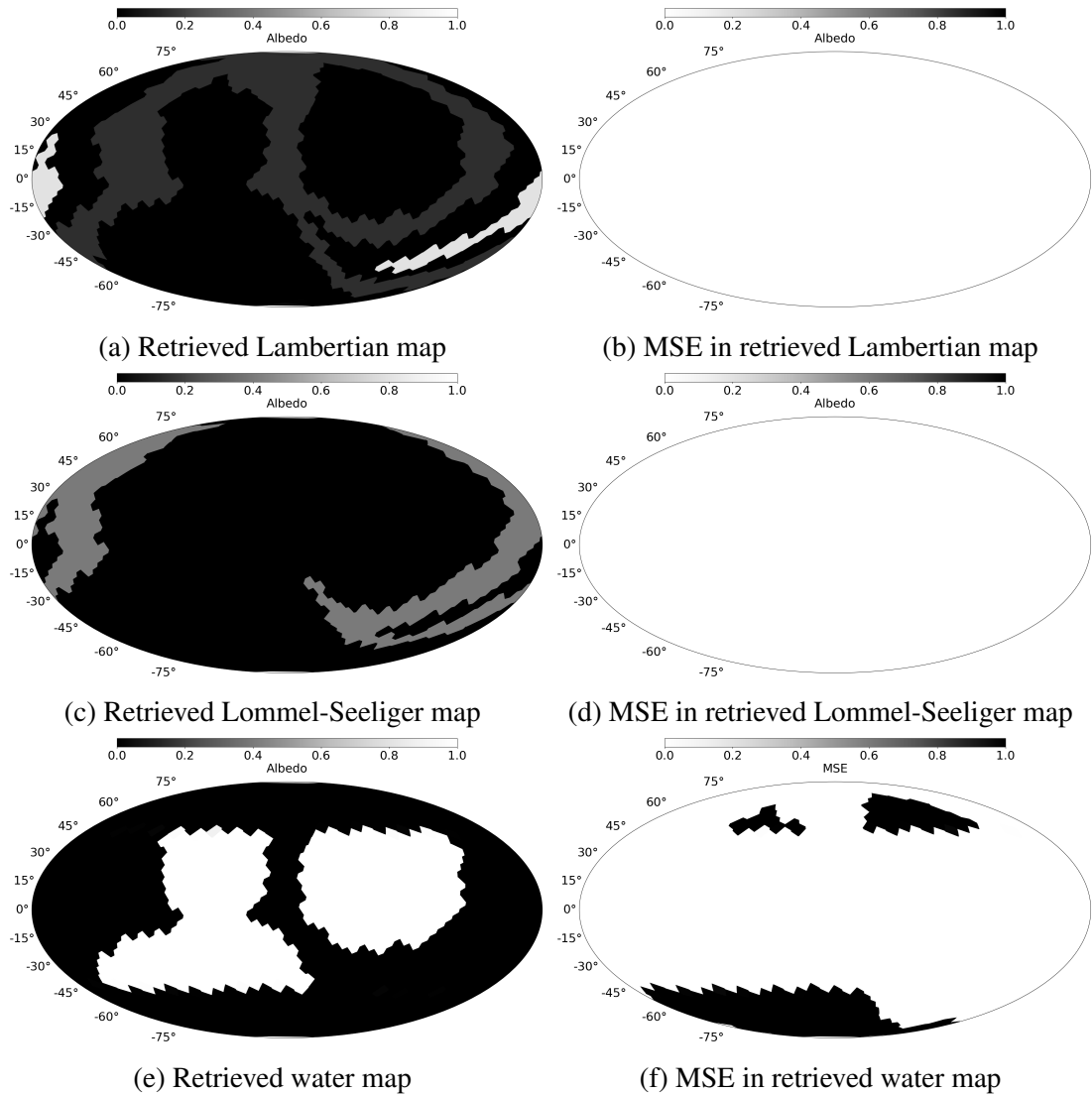


Figure 29: The retrieved albedo maps ((a), (c) and (e)) from the noiseless signal from figure 28 using the method described in section 6.1. The MSE indicating the accuracy of the retrieval is shown in (b), (d) and (f), it is zero in (b) and (d).

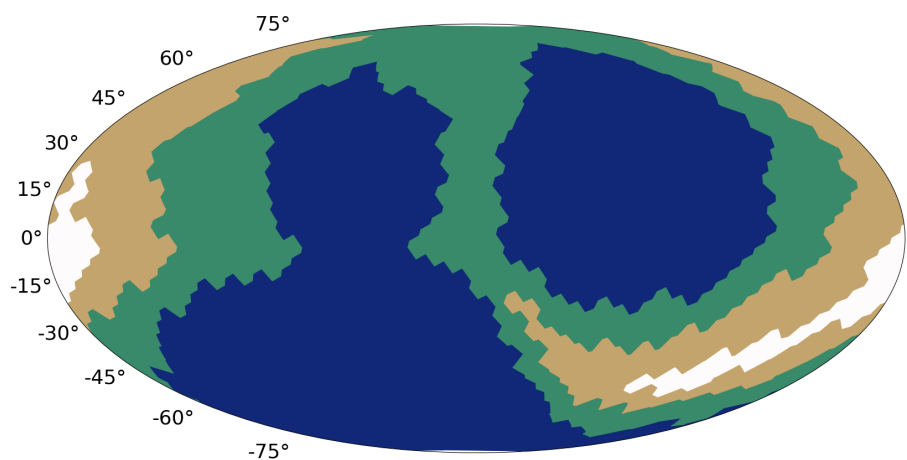


Figure 30: The retrieved planet mapping per surface type from the albedo values for every considered reflection model shown in figure 29. The blue, green, brown and white facets represent water, vegetation, sand desert and snow respectively.

6.3.1. Retrieval with continuous albedo values

In practice, the albedo of a specific surface type can be different for different points on the planet as described in section 3. These albedos applied to multiple reflection models gives them the following albedo vectors: water is kept at the constant albedo vector of $(0, 0, 1)$, vegetation ranges from $(0.1, 0, 0)$ to $(0.3, 0, 0)$, sand ranges from $(0, 0.3, 0)$ to $(0, 0.5, 0)$, and snow ranges from $(0.6, 0, 0)$ to $(0.9, 0, 0)$. The created albedo map from the altitude map of figure 9a is shown in figure 31(a)-(c). From these, the surface map is created using the same method to determine the surface type from the albedo values as with the discrete albedos, but now computing the distance to the mean albedo of a surface type. This is shown in figure 31(d).

From noiseless observation of this planet with equinox $\beta_e = \frac{\pi}{2}$ and obliquity $\beta_o = \frac{\pi}{6}$, the retrieved albedo map is shown in figure 32 with the MSE per reflection type. From the retrieved albedo maps, the surface shown in figure 33 is retrieved.

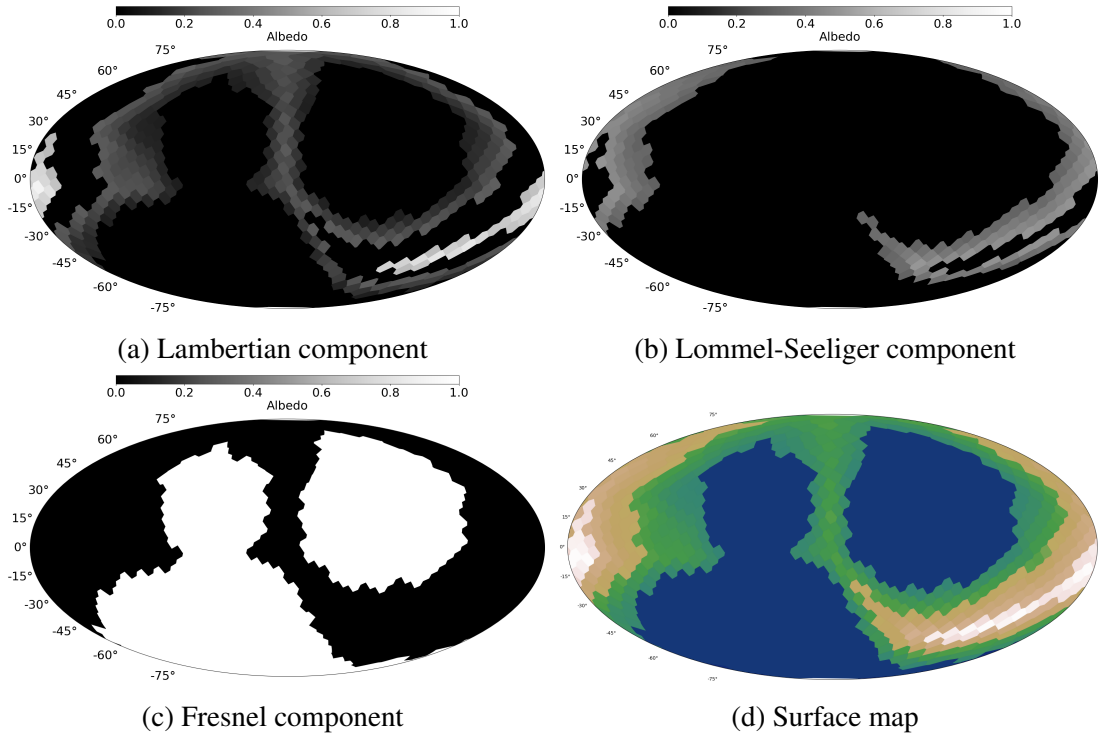


Figure 31: Created albedo maps based on the height map of figure 9a for each considered reflection type for a continuous range of albedo values per surface type in (a)-(c). The combined surface map is shown in (d).

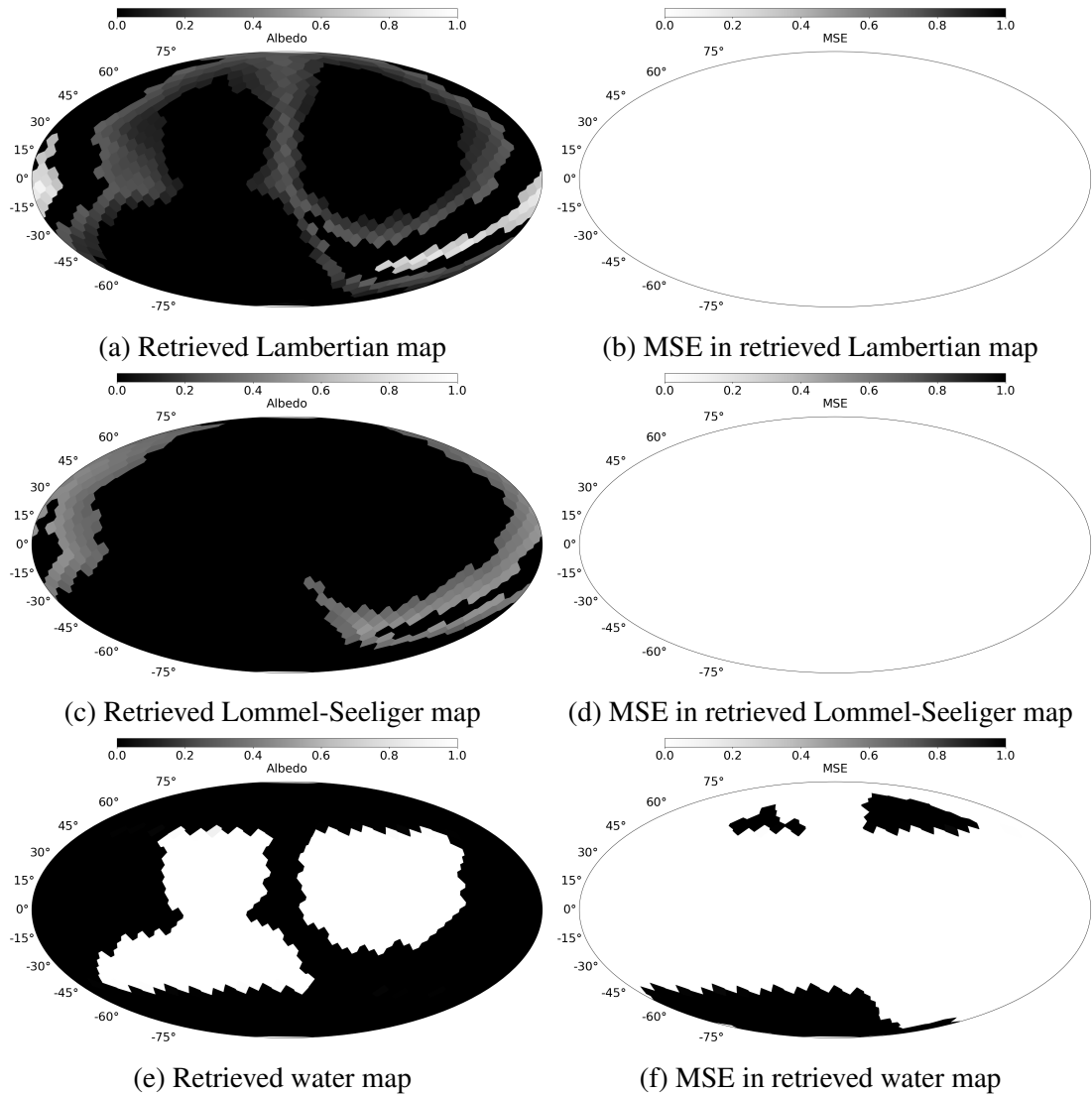


Figure 32: The retrieved albedo maps from the signal generated by the map in figure 31 with 3500 time measurements spread evenly throughout the year where the planet has equinox angle $\beta_e = \frac{\pi}{2}$ and obliquity $\beta_o = \frac{\pi}{6}$.

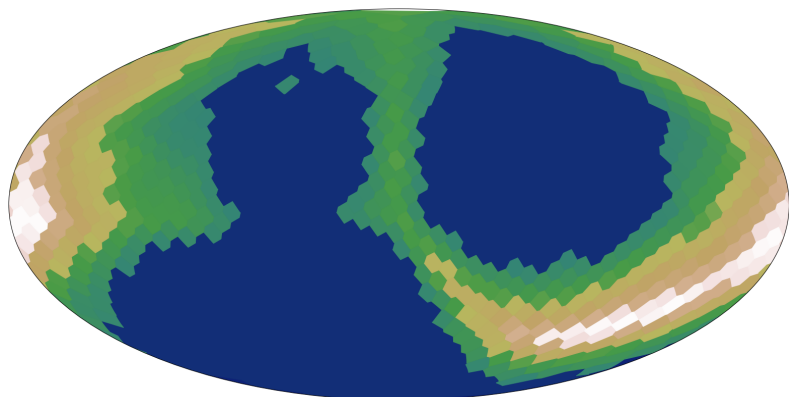


Figure 33: The retrieved planet mapping per surface type from the range of retrieved albedos for every considered reflection model shown in figure 32. The blue, green, brown and white facets represent water, vegetation, sand desert and snow respectively. Darker facets indicate a lower albedo than lighter facets. The original map is shown in figure 31 (d), note that the only incorrectly retrieved facet is a small island in the north of the left ocean.

6.4. Surface map retrieval from signal with shot noise

In the previous paragraphs it has been shown that an exoplanet's map can be retrieved very accurately using spin-orbit tomography when the signal consists of enough measurements in time and there is no noise. In the following paragraphs, the method will be tested on signals with shot noise. The generation of these signals is described in section 5.4. First, the map retrieval is tested for every reflection type individually, then the map retrieval is tested on a planet with different surface types.

6.4.1. Albedo retrieval for individual reflection models with shot noise

To start, the albedo retrieval for individual reflection models with shot noise is investigated. The corresponding light curves are shown in figure 34, from the light curves the albedo maps retrieved with multiple Singular Value Cutoff Ratio's (SVCR's) are shown in figure 35. As mentioned in section 6.1, a key part in the correct retrieval from a noisy signal is the truncation of the pseudo-inverse of the transformation matrix T in the form of a singular value cutoff. As a result of this cutoff, small components of the signal f are rejected. If this cutoff value is too small, anomalies in the signal caused by noise are not filtered out, resulting in an erroneously retrieved map as seen in figure 35 (c)-(e). If this cutoff value is too large, not only will the noise be filtered out of the signal, true information about the surface is also filtered out. This results in an undetailed map retrieval, as shown in figure 35 (i)-(k). The perfect value of the cutoff is one that is as low as possible to retain as much information about the surface as possible, while filtering out the shot noise.

A more detailed analysis of the retrieval quality of albedo maps from a signal with shot noise and the effect of different SVCR's follows. A SVCR of 0.005 is too low, as the retrieved map is dominated by noise for the Lambertian and Lommel-Seeliger reflection. This is expressed in the retrieved map by sharp spikes in albedo values that are unrelated to the original map. The water map shows that the main body of water is retrieved adequately where glint occurs. However, the surface would not be retrieved correctly if the planet would consist of small parts of water or small islands. Since the surface near the equator has many small anomalies, if the true surface is made out of small islands, the anomalies could not be distinguished from the islands. Furthermore, to compare $\text{SVCR} = \frac{1}{14}$ and $\text{SVCR} = 0.25$, it can be noted that these maps are not dominated by noise, because there are no sharp peaks of albedo values. Thus, by the argument made in the previous paragraph, the higher SVCR is preferred, concluding that the best SVCR of these three is $\frac{1}{14}$. It also makes sense that the $\text{SVCR} = \frac{1}{14}$ gives the best retrieval, because the signal to noise ratio of the signal is $\text{SNR}_{\max} \approx 14$ and the cutoff approximately removes values that are smaller than $\frac{1}{14}$ of the maximum value of the signal. The main features of the retrieved Lambertian and Lommel-Seeliger maps are very close to the original map, demonstrating that the map of an exoplanet that is fully described by either of these reflections can be realistically retrieved as long as it satisfies the assumptions made (stationary, earth-twin, etc.).

Furthermore, in figure 35(h), it can be seen that the retrieval of the water map fails at the equator, contrary to the noiseless retrieval. This is caused by the following occurrence; since the planet is tilted towards the observer, the surface at around $\frac{\pi}{6}$ radians from the equator is in the glint when the phase angle is close to $\frac{\pi}{2}$. Conversely, glint around the

equator is only present at small phase angles. Because of the Fresnel coefficient as seen in figure 20, the signal from the glint is weak at small phase angles. Also, small values are truncated out of the signal by the singular value cutoff in the pseudo-inverse of transformation matrix T . Thus in the attempt to filter small noise values, the small intensity of light that is reflected from water at the equator is filtered out of the signal.

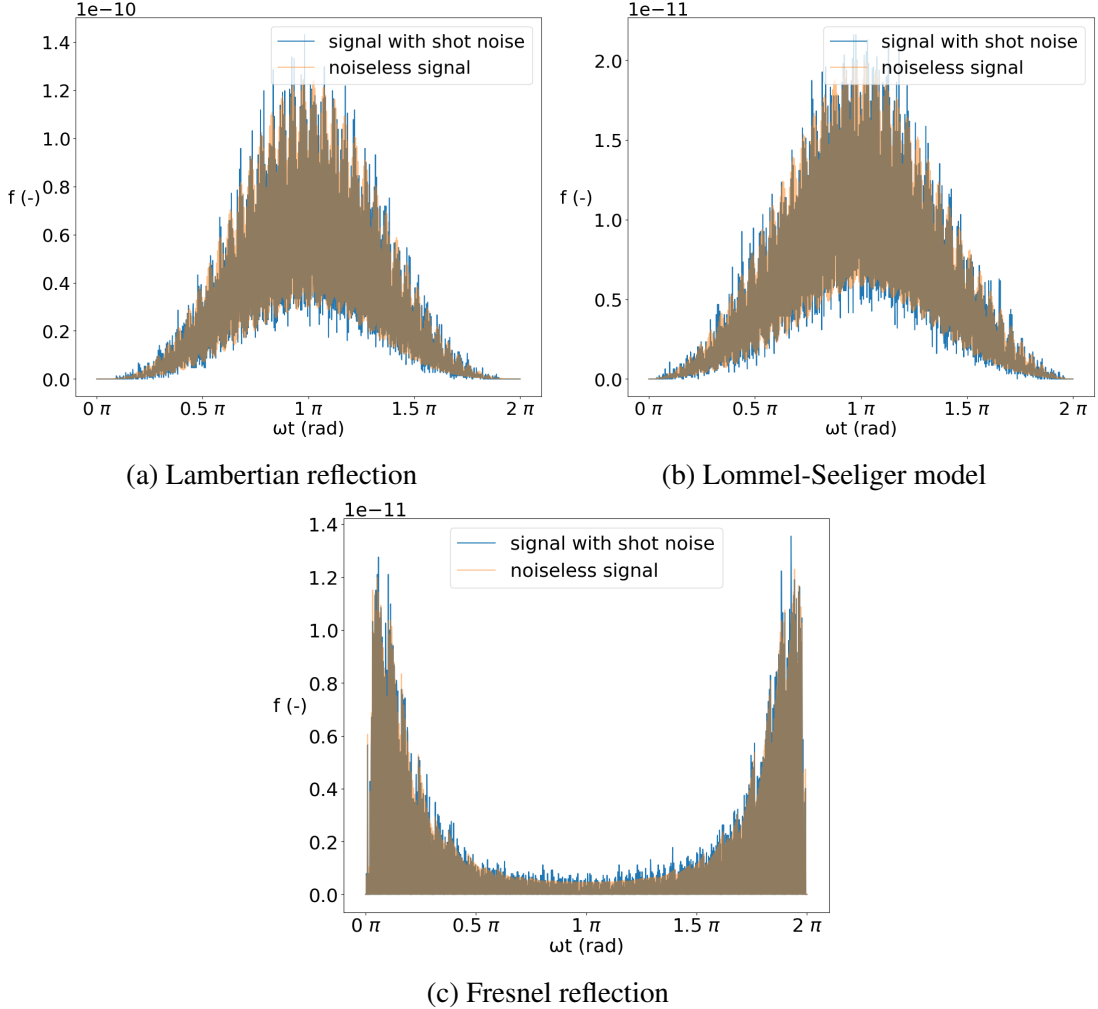


Figure 34: Light curves for edge-on observation of the artificially generated exoplanet shown in figures 35(a) and (b) with shot noise with $\text{SNR} \approx 14$ at the peak of the light curve. The solid blue curves show the noisy signal and the overlaid transparent orange curve shows the noiseless signal. The vertical axis shows the light-intensity relative to the planet's host star and the horizontal axis shows the product of time t and the angular frequency of the planet's orbit ω . Figure (a) shows the light curve when the planet reflects light diffusely, figure (b) shows the light curve when the Lommel-Seeliger law describes the planet's reflection, and figure (c) shows the light curve when the water reflects light by Fresnel reflection and the land does not reflect light. This planet's orbital period equals 365 diurnal periods and it has an equinox angle $\beta_e = \frac{\pi}{2}$ and obliquity $\beta_o = \frac{\pi}{6}$. There are 1500 time measurements spread out evenly over the year.

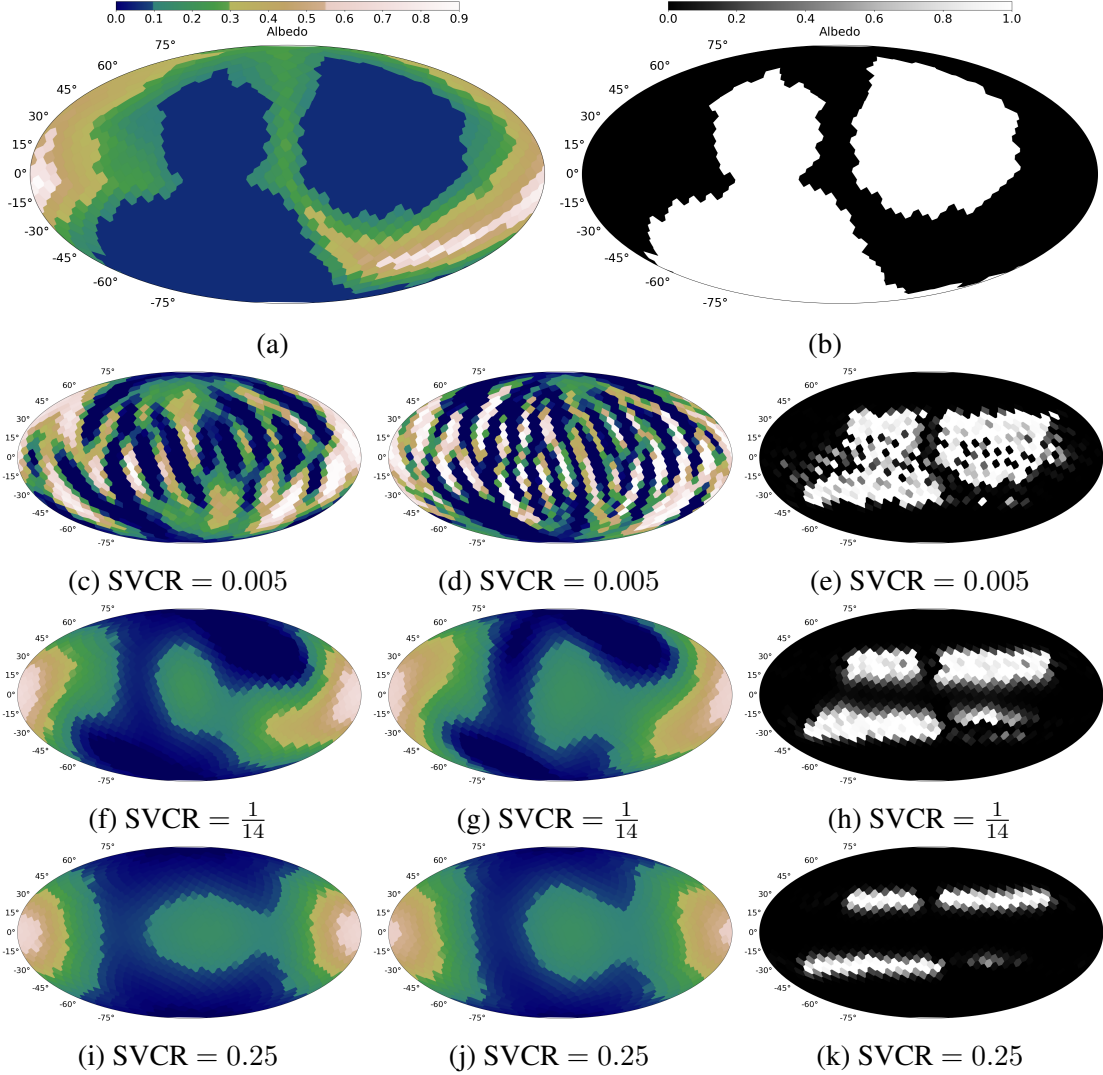


Figure 35: The retrieved albedo maps (c)-(k) from the signal with shot noise generated from a fully Lambertian planet (a) for the retrieved maps (c), (f) and (i), from a planet (a) described fully by the Lommel-Seeliger law for the retrieved maps (d), (g) and (j), and for the planet (b) described by Fresnel reflection for the retrieved maps (e), (h) and (k). The planet has an equinox angle $\beta_e = \frac{\pi}{2}$ and obliquity $\beta_o = \frac{\pi}{6}$. There are 1500 time measurements spread out evenly over the year. Different singular value cutoff ratio's (SVCR) are used, indicated below the retrieved images.

6.4.2. Retrieval of surface map from a signal with shot noise

To extend the results of the previous paragraph to a planet with multiple surface types, the map retrieval described in section 6.3 is performed on a signal with shot noise. This is done for planets with all an equinox of $\beta_e = \frac{\pi}{2}$ and obliquity of respectively $\beta_o = \frac{\pi}{2}, \frac{\pi}{6}, 0$ in order to also gain insight on the retrieval with different tilt angles. Their light curves are shown in figure 36, from these light curves the retrieved albedo and surface maps are shown in figure 37.

Firstly, the effect of obliquity on the retrieval quality is assessed. It is clear that a greater obliquity results in a better quality of the retrieved map, because the retrieved surface map at obliquity $\beta_o = \frac{\pi}{2}$ resembles the original map more than the retrieved

surface at obliquity $\beta_o = 0$ does. To explain this, note that the method used to compute a surface map from a light curve is based on the diurnal and seasonal variations caused by the surface. If these variations are greater, then the map can be retrieved more accurately. In addition, if the obliquity is closer to $\frac{\pi}{2}$, the seasonal changes are larger, thus it makes sense that the retrieval gets better as the obliquity gets closer to $\frac{\pi}{2}$.

Furthermore, it can be noted that the retrieved surface maps only include water and vegetation; sand and snow are not retrieved. This is a result of the retrieved albedo maps of the reflection types. The retrieved Lommel-Seeliger map is approximately zero for all obliquities except $\beta_o = \frac{\pi}{2}$, so almost no facets are retrieved as sand. This is caused by the smaller intensity of Lommel-Seeliger reflection compared to Lambertian reflection as shown in section 4. As a result of the SVCR, apart from noise, also small values are filtered out, resulting in near-zero retrieved Lommel-Seeliger and water maps. Additionally, the Lambertian map only contains small values, causing no facet to be retrieved as snow. This occurs because the signal that is created by the snow originally, can also be caused by a larger diffuse area with lower albedo after filtering the noise.

In an attempt to retrieve non-zero Lommel-Seeliger and water maps, the SVCR is decreased to 0.005, the result of this for the planet with obliquity $\beta_o = \frac{\pi}{6}$ and equinox $\beta_e = \frac{\pi}{2}$ is shown in figure 38. The figure shows that the water map is retrieved with great accuracy at the ocean glint peaks around $\frac{\pi}{6}$ radians from the equator. However, the Lambertian and Lommel-Seeliger maps are polluted by noise, this subsequently explains the inaccurate retrieval of the surface map. Hence, it is not a solution to lower the SVCR for multi-reflectional retrieval. Nevertheless, a lower SVCR can be used to verify that large bodies of liquid are present on the planet around the glint peaks, which would be a great accomplishment if achieved with real data.

In conclusion, for an exoplanet at 25 light-years that is in a twin solar system and has Lambertian surfaces, rocky surfaces can not be retrieved accurately because this either reflects too little light compared to the Lambertian surface or a distinction can not be accurately made between Lambertian reflection and Lommel-Seeliger reflection. This can be solved by reducing the shot noise, this can be done by increasing the measuring time interval or using a larger telescope. Additionally, the general shape of Lambertian surface areas of an exoplanet can be retrieved including rough albedo estimates. Furthermore, the global water map can not be retrieved since glint only occurs at specific bands on the planet, but the presence of water on the glint peak band can be retrieved in detail.

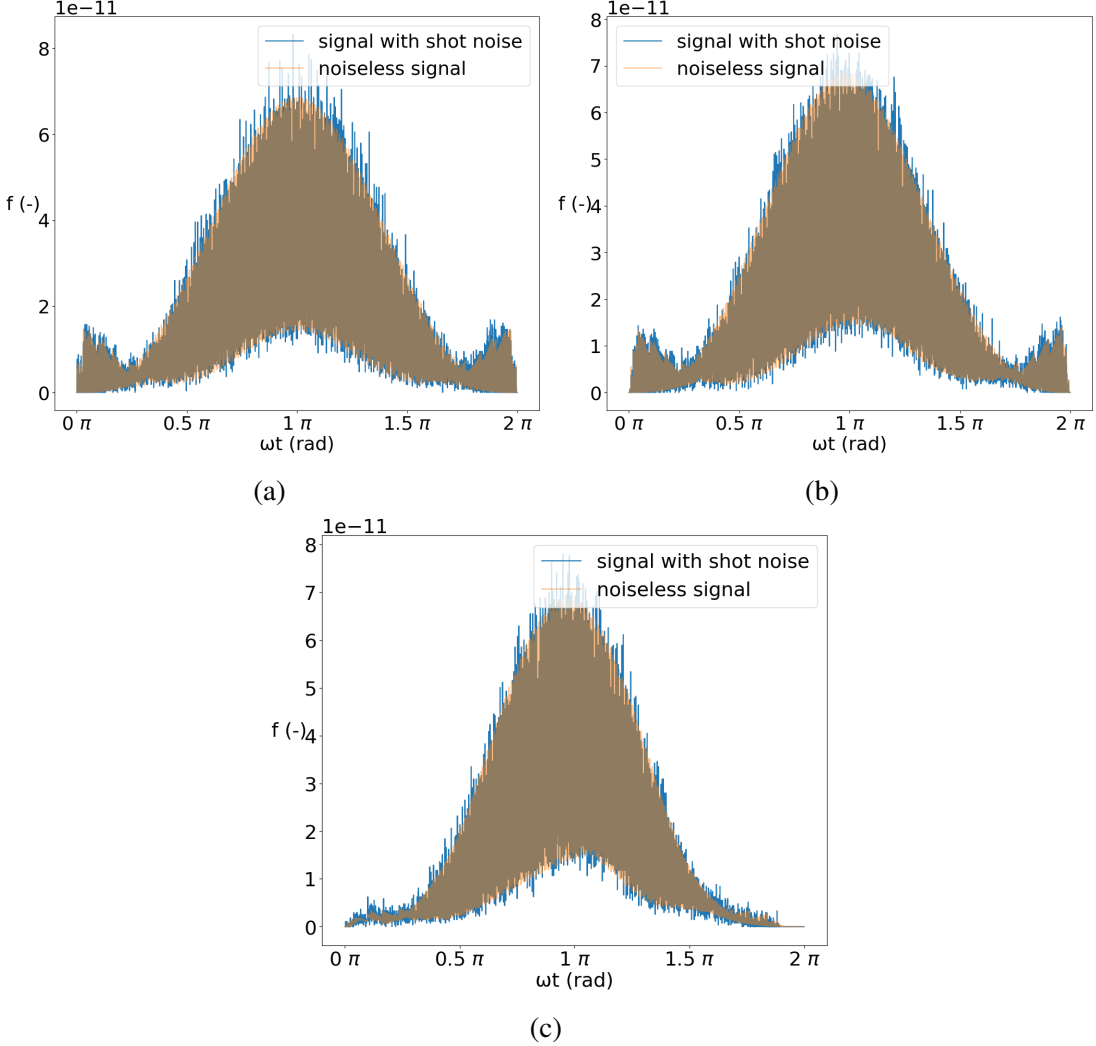


Figure 36: Light curves for edge-on observation of the fictional exoplanet shown in figure 37 row 1 with shot noise with $\text{SNR} \approx 14$ at the peak of the light curve. The solid blue curves show the noisy signal and the overlaid transparent orange curve shows the noiseless signal. The vertical axis shows the light-intensity relative to the planet's host star and the horizontal axis shows the product of time t and the angular frequency of the planet's orbit. The light curves are for the planet with equinox $\beta_e = \frac{\pi}{2}$ and different obliquity: $\beta_o = \frac{\pi}{2}, \frac{\pi}{6}$ and 0 for figure (a), (b) and (c) respectively. For this planet's orbit, a day is 24 hours and there are 365 of these days in its year. There are 3500 time measurements spread out evenly over the year.

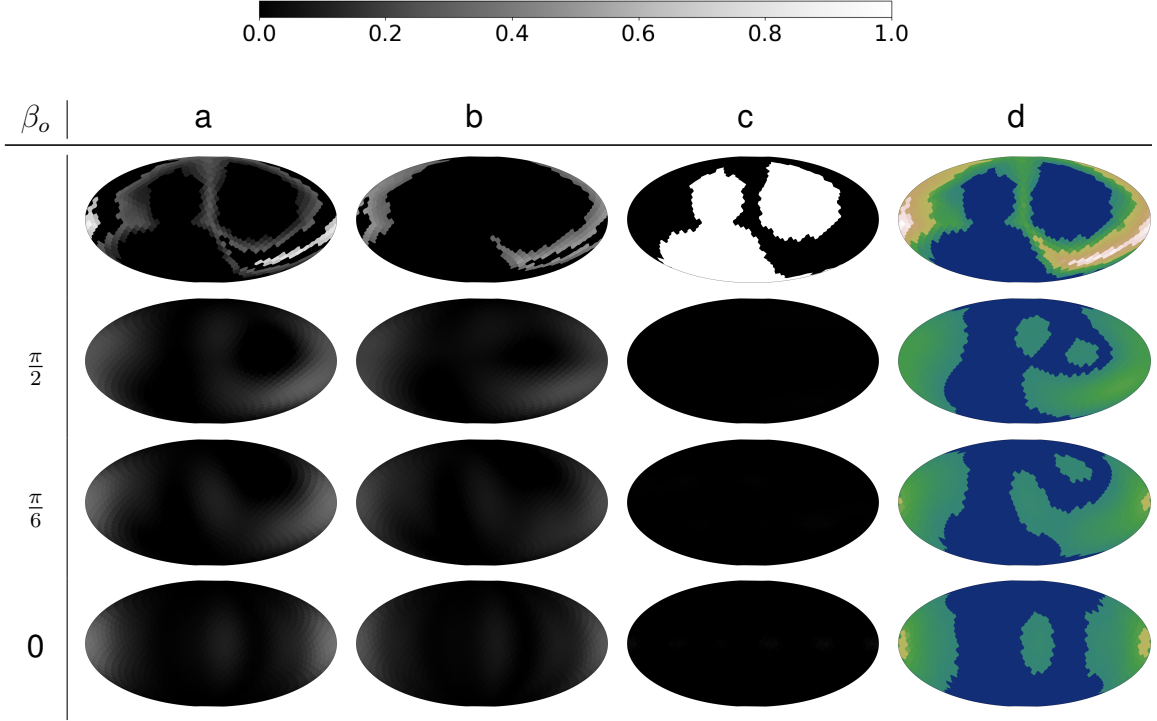


Figure 37: The retrieval of an exoplanet's map from a signal with shot noise for different obliquity angles. The signal consists of 3500 measurements of the exoplanet's intensity spread out evenly across one orbital rotation. The original map is shown in row 1, rows 2, 3 and 4 show retrieval for equinox $\beta_e = \frac{\pi}{2}$ and obliquity $\beta_o = \frac{\pi}{2}, \frac{\pi}{6}, 0$ respectively. Column d shows the surface map, columns a and b respectively show the Lambertian and Lommel-Seeliger components of the surface and column c shows the water map. The colors in the surface maps represent the following surfaces; blue is water, green is vegetation, brown is sand and white is snow. A singular value cutoff ratio of $\frac{1}{14}$ is used to filter the shot noise from the signal.

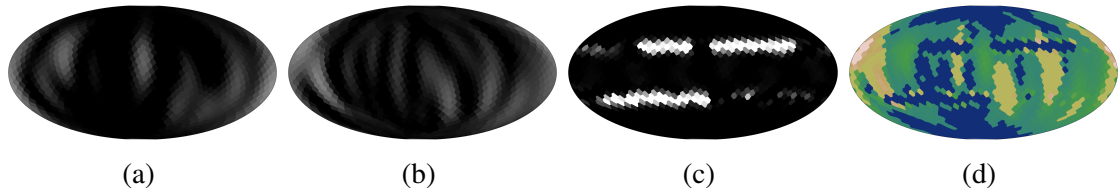


Figure 38: Retrieved albedo maps from a signal with shot noise retrieved with $SVCR = 0.01$ for the Lambertian, Lommel-Seeliger and water map in (a), (b) and (c) respectively, and the surface map resulting from these albedo maps is shown in (d). The signal is computed for the planet shown in figure 37 row 1 with equinox $\beta_e = \frac{\pi}{2}$ and obliquity $\beta_o = \frac{\pi}{6}$. The colors of the retrieved surface are the same as in figure 37.

7. Conclusion

In this thesis, first a near-equal area segmentation of a sphere in flat facets was composed. Then, the surface maps of generated artificial exoplanets were retrieved using spin-orbit tomography with Lambertian, Lommel-Seeliger and Fresnel reflection both separately and collectively. This was first done from an ideal signal and then from a signal with added photon shot noise. The spin-orbit tomography was executed by taking the matrix product of the vector of the albedo map with a so-called transformation matrix, this connects the light curve and the albedo map by a linear transformation. Consequently, the albedo vector was computed from the light curve by taking the matrix product of the Moore-Penrose inverse of the transformation matrix with the light curve.

A few limiting assumptions were made in the method; the exoplanet's surface was assumed to be stationary, inhibiting clouds or changing ice caps, and it was assumed that the surface could be described by any combination of the considered reflection models, so surface types that reflect and scatter light differently were not considered.

The composed near-equal area segmentation of a sphere is the Voronoi diagram of the Fibonacci lattice. For 1001 points on the sphere, the largest facet is only 12% larger than the smallest facet. This is much better than the more traditional segmentation of a sphere by the longitude-latitude lattice, as this difference is 2864 % for this segmentation.

The retrieval of an exoplanet's surface from a signal without noise is close to perfect for both an exoplanet that can be described by one single reflection model (Lambertian, Lommel-Seeliger or Fresnel) and an exoplanet that is described by a combination of these reflection types. In addition, the general shapes of the big features of an exoplanet's surface and its albedo distribution are retrieved very accurately from a signal with shot noise with a signal to noise ratio $SNR \approx 14$ is very successful for individual reflection models. However, when an exoplanet's surface is described by a combination of these reflection models, only the general shape of the water and Lambertian surfaces are retrieved correctly, the surface area with Lommel-Seeliger reflection is not retrieved correctly.

Retrieval quality is better when the planet has a greater obliquity. This is a result of a greater seasonal variation: there is a clearer distinction between information from one hemisphere and the other. Moreover, if the planet has no obliquity, then for edge-on observation a distinction can not be made between the signals from the northern and southern hemisphere. This causes the retrieved map to be symmetric around the equator.

In conclusion, spin-orbit tomography first described by Fujii and Kawahara (2012) that is advanced to include multiple light reflection models, is a realistic way to retrieve an exoplanet's albedo map from its scattered light curve. Thus, when the next-generation telescopes will launch in this decade, their data can be used to infer general information about the surface of exoplanets.

In order to improve the described method, the following recommendations are made:

- The addition of time-dependent components in the planet's map, like clouds and changing ice caps.
- Testing the retrieval quality of different planet surfaces. For example a planet consisting of many small islands, or a fully diffusely reflective planet.
- Testing the retrieval quality with a lower resolution of the light curve. For this

purpose, a lower resolution of the retrieval map could be used, but the original map from which the light curve is created, should retain a higher resolution.

References

- Aurenhammer, F. (1991). Voronoi diagrams - a survey of a fundamental geometric data structure. *ACM Comput. Surv.*, 23(3):345–405.
- Borucki, W. J., Koch, D. G., Basri, G., Batalha, N., Brown, T. M., Bryson, S. T., (...), and Still, M. (2011). Characteristics of planetary candidates observed by kepler ii. analysis of the first four months of data. *The Astrophysical Journal*, 736(1):19.
- Bryson, S., Coughlin, J., Batalha, N. M., Berger, T., Huber, D., Burke, C., Dotson, J., and Mullally, S. E. (2020). A probabilistic approach to kepler completeness and reliability for exoplanet occurrence rates. 159(6).
- Cassan, A., Kubas, D., Beaulieu, J.-P., Dominik, M., Horne, K., Greenhill, J., (...), and Wyrzykowski, K. (2012). One or more bound planets per milky way star from microlensing observations. *Nature*, 481:167–169.
- Dorian (2017). <https://blog.dorian-depriester.fr/latex/tikz/representation-des-angles-deuler-avec-tikz>, last accessed on 14/06/2022.
- Dressing, C. D. and Charbonneau, D. (2015). The occurrence of potentially habitable planets orbiting m dwarfs estimated from the full kepler dataset and an empirical measurement of the detection sensitivity. *The Astronomical Journal*, 807(1).
- Fujii, Y. and Kawahara, H. (2012). Mapping earth analogs from photometric variability: spin–orbit tomography for planets in inclined orbits. *The American Astronomical Society*, 755(2).
- González, Á. (2009). Measurement of areas on a sphere using fibonacci and latitude–longitude lattices. *Mathematical Geosciences*, 42(1):49–64.
- Grant, L. (1987). Diffuse and specular characteristics of leaf reflectance. *Remote Sensing of Environment*, 22(2):309–322.
- Hogan, J. (2006). Planets are round. will that do? *Nature*, 442:724–725.
- Howard, A. W., Marcy, G. W., Johnson, J. A., Fischer, D. A., Wright, J. T., (...), and Ida, S. (2010). The occurrence and mass distribution of close-in super-earths, neptunes, and jupiters. *Science*, 330(6004):653–655.
- Konijnenberg, S., Adam, A. J., and Urbach, H. P. (2021). *Bsc Optics*. TU Delft Open.
- Kunimune, J. (2018). Tissot’s indicatrix.
- Kuusinen, N. (2014). Boreal forest albedo and its spatial and temporal variation. *Dissertationes Forestales*, 2014:1.
- Loera, J. A., Rambau, J., and Santos, F. (2010). *Triangulations*, volume 25. Springer.
- Mayor, M. and Queloz, D. (1995). A jupiter-mass companion to a solar-type star. *Nature*, 378:355–359.

- Mayorga, L. C., Jackiewicz, J., Rages, K., West, R. A., Knowles, B., Lewis, N., and Marley, M. S. (2016). Jupiter's phase variations from cassini: a testbed for future direct-imaging missions. *The Astronomical Journal*, 152(6):209.
- Mogensen, T. ÅE. (2010). Planet map generation by tetrahedral subdivision. In Pnueli, A., Virbitskaite, I., and Voronkov, A., editors, *Perspectives of Systems Informatics*, pages 306–318, Berlin, Heidelberg. Springer Berlin Heidelberg.
- Mungan, C. E. (1998). Bidirectional reflectance distribution functions describing first-surface scattering.
- NSIDC (2020). Thermodynamics: Albedo.
- Przyborski, P. (2002). Blue marble: Land surface, shallow water, and shaded topography.
- Romero-Wolf, A., Bryden, G., Seager, S., Kasdin, N. J., Booth, J., Greenhouse, M., (...), and Stark, C. (2021). Starshade rendezvous: Exoplanet sensitivity and observing strategy.
- Schill, S., Jensen, J., Raber, G., and Porter, D. (2004). Temporal modeling of bidirectional reflection distribution function (brdf) in coastal vegetation. *GIScience Remote Sensing*, 41:116–135.
- Stuger, S. (2021). Exoplanet surface mapping using scattered light curves. Bachelor's thesis, Delft University of Technology.
- Tetzlaff, G. (1983). Albedo of the Sahara. In Cologne Univ. Satellite Meas. of Radiation Budget Parameters p 60-63 (SEE N84-20044 10-46).
- Tuomi, M., Jones, H. R. A., Barnes, J. R., Anglada-Escudé, G., and Jenkins, J. S. (2014). Bayesian search for low-mass planets around nearby M dwarfs – estimates for occurrence rate based on global detectability statistics. *Monthly Notices of the Royal Astronomical Society*, 441(2):1545–1569.
- Uwitonze, A., Huang, J., Ye, Y., Cheng, W., and Li, Z. (2018). Exact and heuristic algorithms for space information flow. *PLOS ONE*, 13:e0193350.
- Winn, J. N., Holman, M. J., Torres, G., McCullough, P., Johns-Krull, C., (...), and Everett, M. (2008). The transit light curve project. IX. evidence for a smaller radius of the exoplanet XO-3b. *The Astrophysical Journal*, 683(2):1076–1084.
- Wright, E., Ladd, D., Petro, N., and Keller, J. (2020). Moon phase and liberation, 2021.

A. Appendix

A.1. Normalisation of BRDF's

With the reflective domain $\mathcal{R} = \{\theta_r \in (0, \frac{\pi}{2}), \psi \in (0, 2\pi)\}$.

For Lambertian reflection $f_{BRDF} = \frac{1}{\pi}$ and the integral over the reflective domain is:

$$\iint_{\mathcal{R}} \frac{1}{\pi} \sin \theta_r \cos \theta_r d\theta_r d\psi = \int_0^{\frac{\pi}{2}} \sin 2\theta_r d\theta_r = 1$$

For the Lommel-Seeliger model $f_{BRDF} = \frac{1}{4\pi(\cos \theta_i + \cos \theta_r)}$ and the integral over the reflective domain is:

$$\begin{aligned} \frac{1}{4\pi} \iint_{\mathcal{R}} \frac{\sin \theta_r \cos \theta_r}{\cos \theta_i + \cos \theta_r} d\theta_r d\psi &= \frac{1}{2} \int_0^{\frac{\pi}{2}} \frac{\sin \theta_r \cos \theta_r}{\cos \theta_i + \cos \theta_r} d\theta_r \\ &= \frac{1}{2} \int_0^{\frac{\pi}{2}} \sin \theta_r d\theta_r - \frac{\cos \theta_i}{2} \int_0^{\frac{\pi}{2}} \frac{\sin \theta_r}{\cos \theta_i + \cos \theta_r} d\theta_r \\ &= \frac{1}{2} - \frac{\cos \theta_i}{2} \int_{1+\cos \theta_i}^{\cos \theta_i} \frac{-1}{u} du \\ &= \frac{1}{2} - \frac{\cos \theta_i}{2} \ln \left(\frac{1 + \cos \theta_i}{\cos \theta_i} \right) \end{aligned}$$

Here the substitution $u = \cos \theta_r + \cos \theta_i$, $du = -\sin \theta_r d\theta_r$ is used. Since $\theta_i \in (-\frac{\pi}{2}, \frac{\pi}{2})$, The last equality is more precise for smaller σ , because the approximation originates from the fact that the integral over the Gaussian is taken over a finite domain. When σ is smaller, the peak of the Gaussian is more sharp inside the integral domain, so the integral is closer to 1.

A.2. Link to GitHub repository

The code used for this project is saved on the following GitHub repository: <https://github.com/SwederB/BEP-Exocartography>.